Impact of Rotational Motion Estimation Errors on Passive Bistatic ISAR Imaging via Backprojection Algorithm

Fabrizio Santi, *Member, IEEE*, Iole Pisciottano, Diego Cristallini, and Debora Pastina, *Member, IEEE*

***Abstract*—This work investigates the impact of motion estimation errors on passive inverse synthetic aperture radar (ISAR) images of rotating targets when the backprojection algorithm (BPA) is employed to focus the data. Accurate target motion estimation can be quite challenging, especially in noncooperative target scenarios. In these cases, BPA is applied under erroneous target kinematics information, entailing defocusing and distortions of the final image product. Starting from the evaluation of the image point spread function (PSF) and the resolution properties of the BPA image under ideally known target motion, it will be analytically shown as, at first order, the PSF under motion estimation errors is approximately a scaled and rotated version of the nominal one. Then, theoretical solutions to predict the location of the scatterers in the image will be provided to characterize in closed form the distortion of the BPA plane. Numerical results under different use cases of practical interest are provided to analyze the level of accuracy required by the motion estimation task for a reliable focus in the challenging passive radar scenario. Experimental results using both terrestrial and satellite signals of opportunity are also provided, showing the general validity of the approach in different passive ISAR systems. The present analysis is not limited to passive radars and it can also be applied to active bistatic radars having limited transmitted bandwidth.**

***Index Terms*—Backprojection algorithm (BPA), bistatic inverse synthetic aperture radar (ISAR), ISAR focusing, motion estimation errors, passive ISAR.**

NOMENCLATURE

Symbol	*Description*
$\boldsymbol{r_x}$	Receiver vector position
$\boldsymbol{t_x}$	Transmitter vector position
d_R	Receiver-to-target distance
d_T	Transmitter-to-target distance
d_b	Transmitter-to-receiver distance
ψ_R^0	Receiver elevation angle
ψ_T^0	Transmitter elevation angle
θ_R^0	Receiver aspect angle
θ_T^0	Transmitter aspect angle
β	Bistatic angle
$\hat{\boldsymbol{\phi}}_R$	Unit vector of the receiver to target line
$\hat{\boldsymbol{\phi}}_T$	Unit vector of the transmitter to target line
$\hat{\boldsymbol{\phi}}_\beta$	Unit vector of the bistatic range resolution direction
$\hat{\boldsymbol{\xi}}$	Unit vector of the Doppler resolution direction
$\boldsymbol{\omega}^0$	Target rotation vector at the image time
ω_x	Roll
ω_y	Pitch
ω_z	Yaw
$\boldsymbol{a}$	Target scatterer vector position
$\psi_{\boldsymbol{\phi}}$	$\hat{\boldsymbol{\phi}}_\beta$ elevation angle
ψ_ξ	$\hat{\boldsymbol{\xi}}$ elevation angle
$\alpha_{\boldsymbol{\phi}}$	Image range resolution direction
α_ξ	Image azimuth resolution direction

I. INTRODUCTION

AT PRESENT, passive radar sensors represent a powerful alternative to conventional active radars for remote surveillance. They exploit the radio frequency (RF) signals already existing in the environment without the need for a dedicated transmitter, therefore enabling lower development and maintenance costs. This facilitates the installation of such systems also in environments where active sensors cannot be installed or are undesired due to their harmful radiations. Passive radar technology has reached today a significant readiness level, with products in the market for the detection, localization, and tracking of moving targets, and researchers are now exploring advanced functionalities to extend the range of potential applications, with passive inverse synthetic aperture radar (ISAR) representing one of the forefront topics [1].

ISAR approaches typically require demanding capabilities for a radar sensor, such as wideband waveforms to achieve fine range resolution and sophisticated signal processing algorithms to achieve well-focused images. These factors made for long-time ISAR imaging an operative mode for active radars only. Nevertheless, the continuous progress of the digital signal processing know-how and the availability of an increasing number of terrestrial and satellite communication signals brought to the advent of the first passive ISAR demonstrations. Most of the research efforts concentrated on the widely available terrestrial TV signals, able to provide acceptable range resolution and relatively high-transmitted power [2], [3]. Other studies considered

Manuscript received 26 June 2023; revised 29 September 2023 and 13 November 2023; accepted 2 December 2023. Date of publication 11 December 2023; date of current version 22 January 2024. *(Corresponding author: Fabrizio Santi.)*

Fabrizio Santi and Debora Pastina are with the Department of Information Engineering Electronics and Telecommunications, Sapienza University of Rome, 00184 Rome, Italy (e-mail: fabrizio.santi@uniroma1.it; debora.pastina@uniroma1.it).

Iole Pisciottano and Diego Cristallini are with the Fraunhofer Institute for High Frequency Physics and Radar Techniques, 53343 Wachtberg, Germany (e-mail: iole.pisciottano@fhr.fraunhofer.de; diego.cristallini@fhr.fraunhofer.de).

Digital Object Identifier 10.1109/JSTARS.2023.3341337

frequency modulation radio [4] and global system for mobile communication [5] illuminators, even though limited at the cross-range profiling due to the very narrowband transmissions, while, for short-range/indoor scenarios, Wi-Fi-based passive ISAR approaches can be found in [6] and [7]. Space-based passive radars benefit, with respect to terrestrial ones, from wider accessibility on the global scale, less reliance on potentially vulnerable infrastructure, and signal reception less sensitive to blockage by obstacles such as in mountain areas. In this framework, digital video broadcasting-satellite (DVB-S) signals represent one of the most interesting options, allowing passive imaging with both fine range and cross-range resolutions, thanks to the availability of transmissions over relatively wide channels in the X/Ku-band [8], [9], [10], [11]. Global navigation satellite signals (GNSS) are another promising alternative, thanks to their global availability and large constellation design. A first introduction and experimental proof-of-concept of GNSS-based passive ISAR has been provided in [12].

Passive ISAR has a number of relevant differences with respect to its active counterpart. First, the geometry is inherently bistatic, as the transmitter and receiver are not colocated. Moreover, the waveforms are not within the control of the user and are not designed for radar purposes. Available bandwidths are generally much narrower than dedicated imaging systems, the ambiguity function may have worse properties, and longer coherent processing intervals (CPIs) can be required to cope with the unfavorable power budget. This latter condition also applies when transmissions in the lower part of the spectrum are exploited, e.g., UHF and VHF, in order to achieve sufficiently fine azimuth resolutions in spite of the relatively long wavelengths [4]. Depending on the particular illuminators, several strategies can be applied to overcome the limitations posed by the challenging passive radar conditions. These typically aim at exploiting the information available over different domains. For example, to increase the range resolution, multichannel combination techniques can be adopted when the allocated spectrum is populated by transmissions over adjacent channels, as often occurs in terrestrial digital television [2], [3]. Multiangle acquisitions may allow to increase the spatial resolution of the image, at the same time allowing for significantly reduced shadowing effects and carrying to a higher signal-to-noise ratio (SNR) [13], [14]. In this framework, a particularly appealing class of illuminators is represented by GNSS, where signals emitted by satellites widely separated in angle can be collected by a single receiver for passive multistatic ISAR tasks [15], [16], [17]. Another interesting approach is capitalizing on the signals collected by differently polarized antennas: different approaches and experimental results about passive polarimetric ISAR can be found in [9] referring to DVB-S illuminators.

The range–Doppler (RD) algorithm is the largest adopted option for passive ISAR focusing. It produces a map of the target scatterers related to their bistatic range and Doppler shifts without precise knowledge of the target rotational motion, as long as the Doppler shift experienced by each scatterer is constant during the CPI. However, as for classification procedures having the images in a homogeneous plane ($m \times m$) is often preferable (especially for the estimation of the target physical dimensions), cross-range scaling is also required. Furthermore, the bistatic geometry induces an additional scaling to be applied to the slant-range dimension to convert the bistatic range into the more meaningful monostatic range [13]. However, the RD algorithm provides its output in an image projection plane (IPP) that depends on the particular illumination and motion conditions. Therefore, RD is not suitable for the direct combination of images taken from a variety of bistatic geometries, which is a fruitful means to overcome the inherent limitations of passive ISAR [14], [15], [16], [19].

Backprojection algorithm (BPA) is an imaging technique that provides a number of benefits over conventional RD. First, wider observation angles can be synthesized regardless of the migration of the scatterers through the Doppler filters. Indeed, it does not make any specific assumption about target motion, representing the optimum filter in the case of perfectly known motion [13]. Even though higher computational complexity than standard RD is typically needed, the increase in the computational power of modern processors is alleviating such an issue. Unlike the IPP of RD, BPA permits imaging in a Cartesian plane representing the target coordinates; therefore, it allows direct extraction of the target geometrical features from the image products. Hence, BPA is particularly suitable when comparing information acquired by different systems. This is the case when direct fusion/comparison of passive images taken from different aspect angles, [19], and/or exploiting multiple illuminators of opportunity, e.g., digital video broadcasting-terrestrial (DVB-T) and DVB-S [20], is conducted.

Previous investigations using BPA for passive ISAR assumed an exact knowledge of the target motion [9], [19], [20]. Although the obtained results showed its potential for passive ISAR imaging, the assumption of perfect knowledge of the target motion was clearly unrealistic. To overcome this issue, in this work, we remove the known target motion assumption by analyzing the robustness of BPA in passive ISAR with respect to motion estimation errors. Particularly, we focus on the impact of inaccuracies of the rotational motion knowledge in general bistatic geometries, and considering different rotation motion types. (Some preliminary results considering a DVB-S-based passive radar have been anticipated in [21] for targets undergoing uniform rotations.) Other contributions in the literature deal with bistatic ISAR [22], [23], [24], and, more specifically, with passive bistatic ISAR [1]. These works focus on the impact of (time-varying) bistatic geometries on ISAR imaging when conventional monostatic RD processors are used. In contrast, the adoption of BPA enables effective image formation regardless of the time-varying behavior of the bistatic angle. Therefore, given the difficulty of achieving fine motion estimates of passive systems, we study the impact of errors in the estimate of the target motion on the quality of the image focused on the Cartesian plane. It is also worth stating that although detailed for the passive radar use where the exploitation of opportunistic waveforms might entail a limited capability to recover accurately the target dynamics, the derivations provided in this work could be applied in principle to any class of bistatic ISAR systems, especially those characterized by coarse range resolution.

In this frame, this article analyzes the effects of estimation errors on both the resolution characteristics and on the distortion affecting the images. For the former task, the bistatic point spread

function (PSF) in the BPA plane will be analytically derived for both the ideal (i.e., error free) and perturbed (i.e., with motion estimation errors) cases. Later, the distortion effects will be evaluated providing closed-form relationships between the error types and the mispositioning of target scatterers in the resulting image. The ultimate goal of this work is to provide passive ISAR users with analytical tools for understanding the robustness of the focusing under different types of operative conditions, so as to establish the level of accuracy to be guaranteed by the motion estimation task. Exemplary numerical results obtained under different use cases are provided to illustrate the tolerance to different motion estimation errors that can be accepted depending on a few possible user needs. Moreover, experimental results using both terrestrial (DVB-T) and satellite (DVB-S) illuminators of opportunity are provided, showing the image quality deterioration in the presence of erroneous kinematic information.

The rest of this article is organized as follows. Section II describes the operative conditions and the BPA focusing, including the resolution properties of the image, under the hypothesis of exactly known target motion. Section III analyzes the impact of motion estimation errors, both in terms of PSF and image distortion. Numerical results for a few exemplary use cases are provided in Section IV. Section V shows experimental results obtained with different illuminators of opportunity. Finally, Section VI concludes this article.

Notations: We introduce here some notations used throughout this article. Scalars are denoted by nonboldface type, vectors by boldface lowercase letters, and matrices by boldface uppercase letters. Superscripts $(\cdot)^T$ and $(\cdot)^*$ denote transpose and complex conjugate, respectively. The dot notation $\dot{x}$ denotes the derivative with respect to the slow time, while the Euclidian norm of vector $\boldsymbol{x}$ is denoted as $\|\boldsymbol{x}\|$. Unit vectors are identified by the hat accent $\hat{\boldsymbol{x}}$. The diacritic sign $\sim$ denotes a quantity modified with respect to its nominal value due to the nonideal knowledge of the target kinematic: let x, $\boldsymbol{x}$, and $\boldsymbol{X}$ be the actual values of a scalar, a vector, and a matrix, respectively, then $\tilde{x}$, $\tilde{\boldsymbol{x}}$, and $\tilde{\boldsymbol{X}}$ denote their corresponding values corrupted by the estimation errors.

II. Passive ISAR Imaging via BPA

A. Operative Conditions and BPA Image

The operative conditions comprise a receiving-only device (Rx), a transmitter of opportunity (Tx), and a target (TgT). We do not make any specific assumption on the particular bistatic geometry or illuminator of opportunity, except it provides a relatively coarse range resolution (i.e., narrowband signals). The target is modeled as a rigid body in the far field composed of a number of scatterers with constant amplitude during the aperture time T_a (CPI). As usual in the ISAR literature, we decompose its motion as the translation of a reference point and the rotation of the target body around that point (target fulcrum). As the focus here is on targets undergoing their own rotations (e.g., ship targets), the former is assumed negligible in the aperture time or already compensated, while the latter gives rise to the Doppler gradient making the imaging effective. Namely, we are assuming that the residual translational motion (if it exists) does not entail residual range and Doppler migration. This is likely fulfilled, because of the coarse range resolution and because the target rotations are usually exploited in scenarios in which target translations do not suffice to provide a Doppler gradient enough to achieve cross-range resolution.

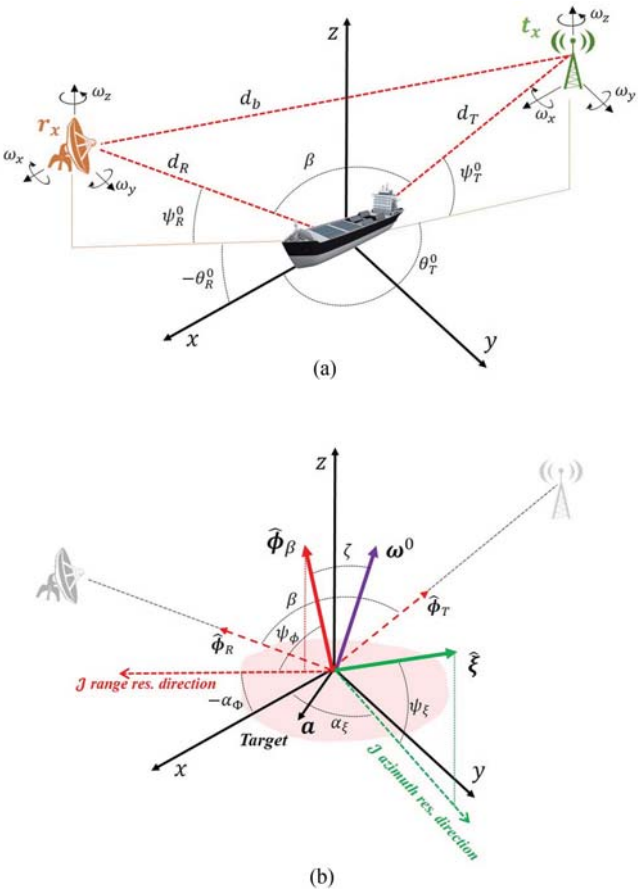

Fig. 1. (a) Passive ISAR geometry with (b) resolution vectors.

Fig. 1(a) shows the considered right-handed $(0, x, y, z)$ reference system, inertial with the target and centered in its fulcrum, namely, x, y, and z axes represent the longitudinal, lateral, and vertical axis, respectively, of the target itself. Fig. 1(b) illustrates the relevant vectors for the subsequent derivations as they will be introduced in this section. For easy use of future reference, Nomenclature lists the main symbols with their description.

Let $u \in [-\frac{T_a}{2}, \frac{T_a}{2}]$ be the variable spanning the slow time. At the image time $u = 0$, d_R, d_T, and d_b are the Rx-to-TgT, Tx-to-TgT, and Tx-to-Rx distances. The target is supposed pitching, rolling, and yawing. Therefore, in the target-fixed reference system, the transmitter and receiver rotate around the target in opposite directions and their instantaneous positions can be written as

$$\begin{aligned} \boldsymbol{r}_{\boldsymbol{x}}(u) &= d_R \boldsymbol{M}_\omega(u)\, \hat{\boldsymbol{\phi}}_R \\ \boldsymbol{t}_{\boldsymbol{x}}(u) &= d_T \boldsymbol{M}_\omega(u)\, \hat{\boldsymbol{\phi}}_T \end{aligned} \tag{1}$$

where $\hat{\boldsymbol{\phi}}_R = [\cos(\theta_R^0)\cos(\psi_R^0), \sin(\theta_R^0)\cos(\psi_R^0), \sin(\psi_R^0)]^T$ and $\hat{\boldsymbol{\phi}}_T = [\cos(\theta_T^0)\cos(\psi_T^0), \sin(\theta_T^0)\cos(\psi_T^0), \sin(\psi_T^0)]^T$ are the unit vectors of the lines Rx-TgT and Tx-TgT, θ_R^0 (respectively θ_T^0) denoting the aspect angle of the receiver (respectively

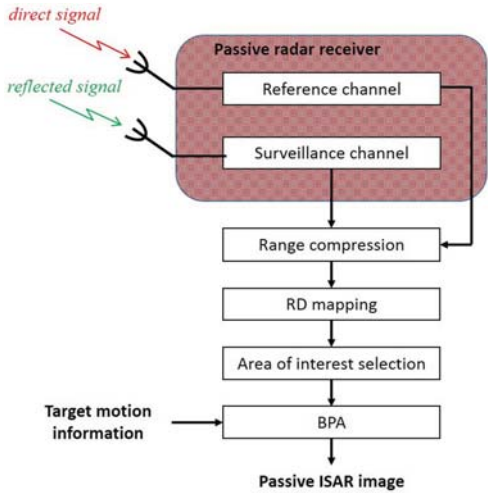

Fig. 2. Passive ISAR processing chain.

transmitter) measured clockwise from the x-axis and ψ_R^0 (respectively ψ_T^0) denoting the receiver (respectively transmitter) elevation angle [see Fig. 1(a)], evaluated at the image time $u = 0$. $\boldsymbol{M}_\omega(u)$ is the instantaneous matrix accounting for the roll, pitch, and yaw motions equal to

$$\begin{aligned}\boldsymbol{M}_\omega(u) &= \boldsymbol{M}_z(u)\,\boldsymbol{M}_y(u)\,\boldsymbol{M}_x(u)\\ &= \begin{bmatrix} C_z & -S_z & 0\\ S_z & C_z & 0\\ 0 & 0 & 1\end{bmatrix}\begin{bmatrix} C_y & 0 & S_y\\ 0 & 1 & 0\\ -S_y & 0 & C_y\end{bmatrix}\begin{bmatrix} 1 & 0 & 0\\ C_x & -S_x & 0\\ S_x & C_x & 0\end{bmatrix}\\ &= \begin{bmatrix} C_yC_z & -C_xS_z + S_xS_yC_z & S_xS_z + C_xC_yC_z\\ C_yS_z & C_xC_z - S_xS_yS_z & C_xS_yS_z - S_xC_z\\ -S_y & S_xC_y & C_xC_y\end{bmatrix}\end{aligned} \tag{2}$$

where $\boldsymbol{M}_x(u)$, $\boldsymbol{M}_y(u)$, and $\boldsymbol{M}_z(u)$ are the instantaneous rotation matrices accounting for roll, pitch, and yaw, $C_\gamma = \cos[\vartheta_\gamma(u)]$ and $S_\gamma = \sin[\vartheta_\gamma(u)]$ and $\vartheta_\gamma(u)$ is the instantaneous angle swept around the $\gamma = x, y, z$ axis. By deriving $\vartheta_\gamma(u)$, $\gamma = x, y, z$, with respect to the slow time u, it is easy to obtain the instantaneous angular velocities $\omega_x(u)$, $\omega_y(u)$, and $\omega_z(u)$, denoting the roll, pitch, and yaw instantaneous rotations that can be collected into the vector $\boldsymbol{\omega}(u) = [\omega_x(u), \omega_y(u), \omega_z(u)]^T$. Considering the possibility of targets observed for significantly long CPIs (as often needed in case of low-power illuminators or signals at lower frequencies), the rotation rate around each axis is expanded in the Taylor series at first order, thus accounting for a constant rotation plus a rate, i.e., $\omega_\gamma \approx \omega_\gamma^0 + \dot{\omega}_\gamma u$, with the apex "0" denoting the value at image time $u = 0$. Overall, the instantaneous rotation vector can be rewritten as

$$\boldsymbol{\omega}(u) \approx \left[\omega_x^0, \omega_y^0, \omega_z^0\right]^T + \left[\dot{\omega}_x,\ \dot{\omega}_y,\ \dot{\omega}_z\right]^T u = \boldsymbol{\omega}^0 + \dot{\boldsymbol{\omega}} u. \tag{3}$$

We assume the receiver to be equipped with a reference channel to collect the direct signal, plus a surveillance channel to collect reflections from the surveyed area. To achieve a focused image of the target in the passive scenario, the following main stages are usually implemented, as sketched in Fig. 2. As typically the illuminators of opportunity operate with signals continuous in time, data reformatting according to the equivalent of fast time and slow time (τ, u) is implemented. This is achieved by segmenting the received data in consecutive batches according to an equivalent pulse repetition interval (PRI), namely, $\tau \in [0, \text{PRI}]$.[1] Hereinafter, we will assume that the fictitious PRI has been chosen sufficiently short to avoid Doppler spectrum folding. After downconversion, for each batch, the data are range compressed by cross correlating the complex envelope of the signal received in the surveillance channel with a replica of the direct signal registered by the reference channel. Then, by Fourier-transforming the slow time, an RD map of the surveyed area is obtained. Here, the target can be detected and the area of interest, containing the target energy, is cropped from the whole map. The resulting cropped map can be interpreted as an unfocused image of the target (if needed, the CPI exploited for ISAR imaging can be extended by juxtaposing data corresponding to consecutive RD maps). Depending on the particular conditions, advanced techniques could be required to detect the target under unfavorable power budget conditions and additional signal processing stages could be needed to remove undesired disturbances, such as clutter and direct path interference [13]. The analysis of the impact of such effects is beyond the scope of this work and it will not be further considered in the following. This means we assume the target is already detected and the motion estimation errors to be the only source of nonideality affecting the focusing.

The last stage is image focusing, aiming at producing a well-focused and interpretable image of the target to enable classification procedures. In our work, this step is performed through BPA, which produces an image in the $(0, x, y, z)$ target reference system by compensating, over a grid, the instantaneous delay and phase according to the available kinematic parameters information. Our implementation of the BPA is as follows (see also [9] and [20]).

Let $\boldsymbol{a} = [x, y, z]^T$ be a hypothesized scatterer belonging to the target body. The signal received from $\boldsymbol{a}$ can be written in the fast-frequency and slow-time domain (f, u) as

$$h_{\boldsymbol{a}}(f, u) = S(f) \exp\left\{-j2\pi (f + f_c)\, \tau_{\boldsymbol{a}}(u)\right\} \tag{4}$$

where $S(f)$ is the spectrum of the transmitted signal after compensation of the phase modulation induced by the data payload content, f_c is the central frequency, and $\tau_{\boldsymbol{a}}(u)$ is the instantaneous time delay. In the geometry under consideration, it is given by

$$\tau_{\boldsymbol{a}}(u) = \frac{\|\boldsymbol{r}_{\boldsymbol{x}}(u) - \boldsymbol{a}\| + \|\boldsymbol{t}_{\boldsymbol{x}}(u) - \boldsymbol{a}\| - d_b}{c} \tag{5}$$

being c the speed of light.

Without loss of generality, let us assume the BPA produces a top-view image of the target at a given height $\bar{z}$. Let $\boldsymbol{\mathcal{I}}(x, y; \bar{z})$ be the backprojected image, this is achieved as

$$\boldsymbol{\mathcal{I}}(x, y; \bar{z}) = \int_{-\frac{B}{2}}^{+\frac{B}{2}} \int_{-\frac{T_a}{2}}^{+\frac{T_a}{2}} h_{\bar{\boldsymbol{a}}}(f, u)\, e^{j2\pi(f+f_c)\tau_{\bar{\boldsymbol{a}}}(u)}\, df\, du \tag{6}$$

where $\bar{\boldsymbol{a}} = [x, y, \bar{z}]^T$ and B is the exploited signal bandwidth. If target kinematics are perfectly known, the BPA correctly

[1] Even though we are assuming a transmitter emitting continuous signals, the derivations provided in this work hold also in the case of pulsed transmissions.

integrates the energy in the fast frequency over the whole aperture time, thus maximizing the image quality as much as possible. The resolution properties of $\boldsymbol{\mathcal{I}}$ will be analyzed in the following sections, while Section III will address the case of motion estimation errors.

B. Image PSF

The resolution properties of the image can be described by means of the generalized ambiguity function (GAF), representing the correlation coefficient between the returns from the target fulcrum $\mathbf{0}$ and a point $\boldsymbol{a}$ in its vicinity [25]

$$\chi(\boldsymbol{a}) = \frac{\iint h_{\mathbf{0}}(f,u)\, h_{\boldsymbol{a}}^{*}(f,u)\, df du}{\sqrt{\iint |h_{\mathbf{0}}(f,u)|^2\, df du}\sqrt{\iint |h_{\boldsymbol{a}}(f,u)|^2 df du}}. \quad (7)$$

By setting $\bar{P}(f) = {P(f)}/{\int P(f) df}$, $P(f)$ being the power spectral density of the transmitted signal, (7) can be rewritten as

$$\chi(\boldsymbol{a}) = \iint \bar{P}(f)\, e^{j2\pi f \tau_d(u)} e^{j2\pi f_c \tau_d(u)} df du \quad (8)$$

where $\tau_d(u)$ is the differential time delay between point $\boldsymbol{a}$ and fulcrum. Accounting for translational motion compensation, without loss of generality we can set $\tau_{\mathbf{0}}(u) = 0$, and therefore, $\tau_d(u) = \tau_{\boldsymbol{a}}(u)$. It is worth to note that since all the scatterers share the same translational velocity, $\tau_d(u)$ is invariant to any residual translational motion.

The two exponential terms in the equation above imply range and Doppler migrations, respectively. Under ideal knowledge of the target kinematics, the range migration experienced over the aperture time will be perfectly compensated by the BPA; therefore, the first exponential term can be simplified as $\exp\{j2\pi f \tau_{\boldsymbol{a}}^0\}$, where apex "0" denotes the value corresponding at the reference instant. At the same time, the Doppler migration will be compensated as well; therefore, the second exponential term becomes $\exp\{j2\pi f_c[\tau_{\boldsymbol{a}}^0 + \dot{\tau}_{\boldsymbol{a}} u]\}$, where $\dot{\tau}_{\boldsymbol{a}}$ is the differential delay rate. By using these positions and neglecting scale factors, (8) simplifies to

$$\chi(\boldsymbol{a}) = \exp\left\{j2\pi f_c \tau_{\boldsymbol{a}}^0\right\}\; p\left(\tau_{\boldsymbol{a}}^0\right)\; \mathrm{sinc}\left(T_a f_c \dot{\tau}_{\boldsymbol{a}}\right). \quad (9)$$

It can be observed as $\chi(\boldsymbol{a})$ is given by the product of three terms: an initial phase, the time response of the signal of opportunity $p(*)$ (specifying the range resolution properties), and a sinc function characterizing the Doppler properties.

While (9) describes the resolution properties in the delay (i.e., range) and Doppler domain, its arguments can be manipulated to have the PSF representation in the Cartesian space. For this purpose, considering the limited size of the targets of interest with respect to the transmitter and receiver to target distances, we can approximate $\tau_{\boldsymbol{a}}(u)$ around the fulcrum arresting the series expansion at the first order

$$\begin{aligned}\tau_{\boldsymbol{a}}(u) &\approx \tau_{\mathbf{0}}(u) + \nabla\tau_{\boldsymbol{a}}(u)_{\boldsymbol{a}=\mathbf{0}}\, \boldsymbol{a} \\ &= -\frac{1}{c}\left(\frac{\boldsymbol{r}_{\boldsymbol{x}}^T(u)\,\boldsymbol{a}}{d_R} + \frac{\boldsymbol{t}_{\boldsymbol{x}}^T(u)\,\boldsymbol{a}}{d_T}\right) \\ &= -\frac{2\cos\left(\beta/2\right)}{c}\hat{\boldsymbol{\phi}}_{\beta}^T \boldsymbol{M}_{\omega}^T(u)\,\boldsymbol{a} \end{aligned} \quad (10)$$

where ∇ is the vector differential operator and $(\hat{\boldsymbol{\phi}}_R + \hat{\boldsymbol{\phi}}_T) = 2\cos(\beta/2)\hat{\boldsymbol{\phi}}_{\beta}^T$, where β is the bistatic angle and $\hat{\boldsymbol{\phi}}_{\beta}$ is the unit vector lying on its bisector [see Fig. 1(b)]. Then, (10) can further be expanded in the Taylor series around the image time. Arresting the series expansion at the second order

$$\begin{aligned}\tau_{\boldsymbol{a}}(u) &\approx \tau_{\boldsymbol{a}}^0 + \dot{\tau}_{\boldsymbol{a}}^0 u + \frac{1}{2}\ddot{\tau}_{\boldsymbol{a}}\, u^2 \\ &= -\frac{2\cos(\beta/2)}{c}\hat{\boldsymbol{\phi}}_{\beta}^T\left(\boldsymbol{M}_{\omega}^{0T} + \dot{\boldsymbol{M}}_{\omega}^T u + \ddot{\boldsymbol{M}}_{\omega}^T \frac{u^2}{2}\right)\boldsymbol{a}\end{aligned} \quad (11)$$

where $\boldsymbol{M}_{\omega}^0 = \boldsymbol{M}_{\omega}(u=0)$, $\dot{\boldsymbol{M}}_{\omega} = \left(\frac{\partial \boldsymbol{M}_{\omega}(u)}{\partial u}\right)_{u=0}$, and $\ddot{\boldsymbol{M}}_{\omega} = \left(\frac{\partial^2 \boldsymbol{M}_{\omega}(u)}{\partial u^2}\right)_{u=0}$ (for ease of reference, the derivations of $\dot{\boldsymbol{M}}_{\omega}$ and $\ddot{\boldsymbol{M}}_{\omega}$ are included in Appendix A).

As $\boldsymbol{M}_{\omega}^0$ coincides with the identity matrix, the constant term is immediately obtained as

$$\tau_{\boldsymbol{a}}^0 = -\frac{2\cos\left(\beta/2\right)}{c}\hat{\boldsymbol{\phi}}_{\beta}^T\boldsymbol{a}. \quad (12)$$

The delay rate is given by

$$\dot{\tau}_{\boldsymbol{a}} = -\frac{2\cos\left(\beta/2\right)}{c}\left(\boldsymbol{\omega}^0 \times \hat{\boldsymbol{\phi}}_{\beta}\right)^T\boldsymbol{a} \quad (13)$$

where $\times$ denotes the cross product. Let ζ be the angle between $\boldsymbol{\omega}^0$ and $\hat{\boldsymbol{\phi}}_{\beta}$, then the cross product in (13) can be rewritten as $\|\boldsymbol{\omega}^0\|\sin(\zeta)\hat{\boldsymbol{\xi}}$, where $\hat{\boldsymbol{\xi}}$ is the unit vector normal to the plane containing $\boldsymbol{\omega}^0$ and $\hat{\boldsymbol{\phi}}_{\beta}$ [see Fig. 1(b)], carrying to

$$\dot{\tau}_{\boldsymbol{a}} = -\frac{\omega_{\mathrm{Eff}}}{c}\hat{\boldsymbol{\xi}}^T\boldsymbol{a} \quad (14)$$

where $\omega_{\mathrm{Eff}} = 2\cos(\beta/2)\|\boldsymbol{\omega}^0\|\sin(\zeta)$.

For ease of future reference when defining the model of motion errors in Section III, the second-order term is also derived. Considering the derivation of $\ddot{\boldsymbol{M}}_{\omega}$ (see appendix A), $\ddot{\tau}_{\boldsymbol{a}}$ is equal to

$$\ddot{\tau}_{\boldsymbol{a}} = -\frac{2\cos\left(\beta/2\right)}{c}\left(\hat{\boldsymbol{\phi}}_{\beta}^T\boldsymbol{\Omega} + \left(\dot{\boldsymbol{\omega}} \times \hat{\boldsymbol{\phi}}_{\beta}\right)^T\right)\boldsymbol{a} \quad (15)$$

where $\boldsymbol{\Omega}$ is a lower triangular matrix defined as

$$\boldsymbol{\Omega} = \begin{bmatrix} -{\omega_y^0}^2 - {\omega_z^0}^2 & 0 & 0 \\ 2\omega_x^0\omega_y^0 & -{\omega_x^0}^2 - {\omega_z^0}^2 & 0 \\ 2\omega_x^0\omega_z^0 & 2\omega_y^0\omega_z^0 & -{\omega_x^0}^2 - {\omega_y^0}^2 \end{bmatrix}. \quad (16)$$

By using (12) and (14) in (9), the passive ISAR image PSF after ideal BPA focusing as a function of the spatial coordinates is obtained as

$$\chi(\boldsymbol{a}) = p\left[2\cos\left(\frac{\beta}{2}\right)\hat{\boldsymbol{\phi}}_{\beta}^T\boldsymbol{a}\right]\mathrm{sinc}\left[\frac{T_a}{\lambda}\omega_{\mathrm{Eff}}\hat{\boldsymbol{\xi}}^T\boldsymbol{a}\right] \quad (17)$$

being λ the wavelength and where the initial phase term has been omitted.

For the sake of simplicity, we set the BPA output grid to $\bar{z} = 0$ (hereinafter referred to as the ground plane). Let K be the number of target scatterers, image $\boldsymbol{\mathcal{I}}$ will be the coherent

superimposition of the K PSFs (each scaled for the corresponding scatterer complex reflectivity) evaluated at the ground plane level and centered in the kth positions $\bar{\boldsymbol{a}}_k = [\bar{x}_k \quad \bar{y}_k]^T$, representing the position on the ground plane of the scatterer with vector position $\boldsymbol{a}_k = [x_k \quad y_k \quad z_k]^T$. For those scatterers belonging to the ground plane, i.e., $\boldsymbol{a}_k = [x_k \quad y_k \quad 0]^T$, $\bar{\boldsymbol{a}}_k = \boldsymbol{a}_{k_{\setminus z}}$, where the subscript $\setminus z$ denotes the elision of the z component. In contrast, for scatterers lying outside the ground plane, i.e., $\boldsymbol{a}_k = [x_k \quad y_k \quad z_k \neq 0\ ]^T$, $\bar{\boldsymbol{a}}_k$ is generally different from $\boldsymbol{a}_{k_{\setminus z}}$. The position of the scatterer in the image can be calculated considering that both the vectors $\boldsymbol{a}_k$ and $[\bar{\boldsymbol{a}}_k^T, 0]^T$ belong to the same isorange and the same iso-Doppler lines. Therefore, $\bar{\boldsymbol{a}}_k$ can be calculated by solving the following linear system:

$$\begin{cases} \hat{\boldsymbol{\phi}}_\beta^T \boldsymbol{a}_k = \hat{\boldsymbol{\phi}}_\beta^T \left[\bar{\boldsymbol{a}}_k^T, 0\right]^T \\ \hat{\boldsymbol{\xi}}^T \boldsymbol{a}_k = \hat{\boldsymbol{\xi}}^T \left[\bar{\boldsymbol{a}}_k^T, 0\right]^T \end{cases}. \tag{18}$$

Namely

$$\bar{\boldsymbol{a}}_k = \begin{bmatrix} \hat{\boldsymbol{\phi}}_{\beta_{\setminus z}}^T \\ \hat{\boldsymbol{\xi}}_{\setminus z}^T \end{bmatrix}^{-1} \begin{bmatrix} \hat{\boldsymbol{\phi}}_\beta^T \\ \hat{\boldsymbol{\xi}}^T \end{bmatrix} \boldsymbol{a}_k = \boldsymbol{P}\boldsymbol{a}_k \tag{19}$$

where $\boldsymbol{P}$ is the $[2 \times 3]$ matrix relating the positions of the scatterers in $\mathbb{R}^3$ to their positions in the image. (If BPA produces an image at a height $\bar{z} \neq 0$, matrix $\boldsymbol{P}$ can be obtained by replacing in (18) $[\bar{\boldsymbol{a}}_k^T, 0]$ with $[\bar{\boldsymbol{a}}_k^T, \bar{z}]$.)

C. Image Resolution Properties

The couple $(\hat{\boldsymbol{\phi}}_\beta, \hat{\boldsymbol{\xi}})$ sets the bistatic IPP, where $\hat{\boldsymbol{\phi}}_\beta$ and $\hat{\boldsymbol{\xi}}$ define the bistatic range and azimuth resolution directions, respectively. Particularly, on the IPP, from (17), it is easy to see that the range and azimuth resolutions of the system (without loss of generality evaluated at – 3 dB) are given by, respectively

$$\rho_{\boldsymbol{\phi}} = k_p \frac{c}{2\cos\left(\beta/2\right) B} \tag{20}$$

$$\rho_\xi = 0.886 \frac{\lambda}{\omega_{\text{Eff}} T_a} \tag{21}$$

where B is the exploited signal bandwidth of the illuminator of opportunity and k_p is a factor accounting for the shape of $p(*)$. However, unlike RD or polar format algorithms, BPA produces an image on a plane generally not coinciding with the IPP. Let $\alpha_{\boldsymbol{\phi}}$ and α_ξ be the directions of the projections of $\hat{\boldsymbol{\phi}}_\beta$ and $\hat{\boldsymbol{\xi}}$ on the ground plane (measured counterclockwise from the x-axis), representing the image range and azimuth resolution directions, respectively, and let $\psi_{\boldsymbol{\phi}}$ (respectively ψ_ξ) be the angle between $\hat{\boldsymbol{\phi}}_\beta$ (respectively $\hat{\boldsymbol{\xi}}$) and the ground plane [see Fig. 1(b)]. The values of the image range and azimuth resolutions can be obtained as

$$\rho_{\alpha_{\boldsymbol{\phi}}} = \rho_{\boldsymbol{\phi}} / \cos\left(\psi_{\boldsymbol{\phi}}\right) \tag{22}$$

$$\rho_{\alpha_\xi} = \rho_\xi / \cos\left(\psi_\xi\right). \tag{23}$$

It is worth to point out that in the bistatic SAR case, range and azimuth resolution directions are generally not orthogonal [25]. In contrast, in the ISAR framework considered here, $\hat{\boldsymbol{\phi}}_\beta$ and $\hat{\boldsymbol{\xi}}$ are orthogonal by construction, as it results from the cross product in (13). Nevertheless, because of the projections in (22) and (23), ground range and ground azimuth resolution directions $\alpha_{\boldsymbol{\phi}}$ and α_ξ are generally not orthogonal, and therefore, $\rho_{\alpha_{\boldsymbol{\phi}}}$ and ρ_{α_ξ} cannot be proper indicators of the image resolution properties, which are in the scope of the resolution ellipse. This ellipse is defined as the locus of points for which on the ground plane it results $|\chi(\boldsymbol{a})| = 1/\sqrt{2}$ (-3 dB resolution) and its major and minor axes, ρ_{MAX} and ρ_{min}, respectively, define the worst and the best value of the spatial resolution. The resolution ellipse is evaluated as [26]

$$|\chi(\boldsymbol{\rho})| = \left| p\left(2\cos\left(\frac{\beta}{2}\right)\hat{\boldsymbol{\phi}}_\beta^T \boldsymbol{\rho}\right) \text{sinc}\left(\frac{T_a}{\lambda}\omega_{\text{Eff}}\hat{\boldsymbol{\xi}}^T \boldsymbol{\rho}\right)\right| = \frac{1}{\sqrt{2}} \tag{24}$$

where $\boldsymbol{\rho} = [\frac{\rho_\alpha}{2}\cos(\alpha), \frac{\rho_\alpha}{2}\sin(\alpha), 0]^T$, with $\alpha \in [0, 2\pi)$. Solving (24) for each α, we can get the resolution parameter $\rho_\alpha(\alpha)$ describing as the spatial resolution varies with the direction α; the directions and the corresponding values of the best and worst spatial resolutions in the BPA plane are, therefore, obtained as

$$\begin{cases} \alpha_{\text{min}} = \underset{\alpha\in[0,\pi)}{\arg\min}\left\{\rho_\alpha(\alpha)\right\} \rightarrow \rho_{\text{min}} = \rho_\alpha(\alpha_{\text{min}}) \\ \alpha_{\text{MAX}} = \underset{\alpha\in[0,\pi)}{\arg\max}\left\{\rho_\alpha(\alpha)\right\} \rightarrow \rho_{\text{MAX}} = \rho_\alpha(\alpha_{\text{MAX}}) \end{cases} \tag{25}$$

III. Impact of Motion Estimation Errors

So far, we assumed perfect knowledge of system topology. Namely, with reference to Fig. 1, we assumed perfect knowledge of the relative Tx, Rx, and TgT positions (i.e., in the target-fixed reference system of the vector positions $\boldsymbol{t}_{\boldsymbol{x}}$ and $\boldsymbol{r}_{\boldsymbol{x}}$) as well as the target dynamics. However, this information must be generally recovered directly from the received data and is, therefore, subject to nonidealities. Errors on the vector positions $\boldsymbol{t}_{\boldsymbol{x}}$ and $\boldsymbol{r}_{\boldsymbol{x}}$ entail estimation errors on the bistatic angle and on the direction of the range resolution unit vector. However, in typical surveillance scenarios, the inaccuracy of the relative target position is much lower than its distance from the transmitter and receiver. Therefore, estimation errors on β and $\hat{\boldsymbol{\phi}}_\beta$ can be usually neglected. Also, variations of the bistatic angle during the aperture time could be neglected, since we only consider targets undergoing relatively slow translations and rotations around their fulcrum. However, while the time-varying behavior of the bistatic angle can significantly affect focusing performance in the case of RD processors [22], [23], [24], BPA does not make any specific assumption on the motion characteristics and can, therefore, handle such a case.

Major sources of nonideality affecting the BPA data focusing are the estimation errors on the target rotation vector. Indeed, $\boldsymbol{\omega}$ vector can significantly change its orientation among different frames and it can be characterized by nonuniform speed during the selected aperture time [24], [27]. Its estimation is typically quite challenging even for active radar systems and, in the passive ISAR framework, the lack of proper power budget and dedicated waveform design can worsen significantly the situation.

Understanding how residual rotational motion estimation errors affect the final image product may allow setting proper

bounds on the required accuracy of the motion estimation module in order to guarantee a reliable interpretation of the images and their proper exploitation. To this purpose, in this section, after introducing a straightforward model for the motion errors, we will derive the PSF of the image when BPA works under nonexact knowledge of the target motion; then, distortion effects caused by such inaccuracies will be derived in closed form.

A. Image PSF and Resolution Properties Under Motion Estimation Errors

Let $\delta\boldsymbol{\omega}$ be the rotation motion estimation error, comprising a constant and a time varying part $\delta\boldsymbol{\omega}^0 = [\delta\omega_x, \delta\omega_y, \delta\omega_z]^T$ and $\delta\dot{\boldsymbol{\omega}} = [\delta\dot{\omega}_x,\ \delta\dot{\omega}_y,\ \delta\dot{\omega}_z]^T$, respectively, where $\delta\omega_\gamma$ and $\delta\dot{\omega}_\gamma$ ($\gamma = x, y, z$) denote the errors on the single components. Therefore, the estimated rotation vector $\tilde{\boldsymbol{\omega}}$ can be written as

$$\tilde{\boldsymbol{\omega}} = \tilde{\boldsymbol{\omega}}^0 + \widetilde{\dot{\boldsymbol{\omega}}}\, u \ = \left(\boldsymbol{\omega}^0 + \delta\boldsymbol{\omega}^0\right) + \left(\dot{\boldsymbol{\omega}} + \delta\dot{\boldsymbol{\omega}}\right) u. \tag{26}$$

Consequently, an instantaneous time delay $\tilde{\tau}_{\boldsymbol{a}}(u) \neq \tau_{\boldsymbol{a}}(u)$ is injected into the "BPA focusing" block in Fig. 2 and the resulting image is written as

$$\widetilde{\boldsymbol{\mathcal{I}}}(x, y; \bar{z}) = \int_{-\frac{B}{2}}^{+\frac{B}{2}} \int_{-\frac{T_a}{2}}^{+\frac{T_a}{2}} h_{\boldsymbol{a}}(f, u)\, e^{j2\pi(f+f_c)\tilde{\tau}_{\boldsymbol{a}}(u)}\, df du. \tag{27}$$

Likewise the actual instantaneous time delay, also $\tilde{\tau}_{\boldsymbol{a}}(u)$, can be expanded in the Taylor series giving rise to

$$\tilde{\tau}_{\boldsymbol{a}}(u) \approx \tau_{\boldsymbol{a}}^0 + \widetilde{\dot{\tau}}_{\boldsymbol{a}} u + \widetilde{\ddot{\tau}}_{\boldsymbol{a}} \frac{u^2}{2} \tag{28}$$

where the constant term coincides with the actual one as it does not depend on the rotation vector.

By replacing $\boldsymbol{\omega}^0$ with $\tilde{\boldsymbol{\omega}}^0$ in (13), the apparent delay rate can be immediately obtained as

$$\widetilde{\dot{\tau}}_{\boldsymbol{a}} = -\frac{2\cos(\beta/2)}{c}\left(\left(\boldsymbol{\omega}^0 + \delta\boldsymbol{\omega}^0\right) \times \hat{\boldsymbol{\phi}}_\beta\right)^T \boldsymbol{a} = \dot{\tau}_{\boldsymbol{a}} + \delta\dot{\tau}_{\boldsymbol{a}}. \tag{29}$$

The apparent derivative of the delay rate can be evaluated by replacing in (15) the matrix $\boldsymbol{\Omega}$ and the vector $\dot{\boldsymbol{\omega}}$ with their apparent versions. Matrix $\tilde{\boldsymbol{\Omega}}$ can be obtained from (16) by replacing in each of its entry ω_γ^0 with $\omega_\gamma^0 + \delta\omega_\gamma^0$. Thereby, it is easy to verify that $\tilde{\boldsymbol{\Omega}}$ can be written as

$$\tilde{\boldsymbol{\Omega}} = \boldsymbol{\Omega} + \delta\boldsymbol{\Omega} \tag{30}$$

where matrix $\delta\boldsymbol{\Omega}$ denotes the error term. Therefore, we can write

$$\begin{aligned}\widetilde{\ddot{\tau}}_{\boldsymbol{a}} &= -\frac{2\cos\left(\beta/2\right)}{c}\left(\hat{\boldsymbol{\phi}}_\beta^T\left(\boldsymbol{\Omega} + \delta\boldsymbol{\Omega}\right) + \left(\left(\dot{\boldsymbol{\omega}} + \delta\dot{\boldsymbol{\omega}}\right) \times \hat{\boldsymbol{\phi}}_\beta\right)^T\right)\boldsymbol{a} \\ &= \ddot{\tau}_{\boldsymbol{a}} + \delta\ddot{\tau}_{\boldsymbol{a}}.\end{aligned} \tag{31}$$

Overall, because of the error vector $\delta\boldsymbol{\omega}$, an instantaneous error $\delta\tau_{\boldsymbol{a}}(u) = \delta\dot{\tau}_{\boldsymbol{a}} u + \delta\ddot{\tau}_{\boldsymbol{a}} \frac{u^2}{2}$ must be taken into account in the BPA image formation procedure and the resulting image (27) can be rewritten as

$$\widetilde{\boldsymbol{\mathcal{I}}}(x, y; \bar{z}) = \int_{-\frac{B}{2}}^{+\frac{B}{2}} \int_{-\frac{T_a}{2}}^{+\frac{T_a}{2}} S(f)\ e^{j2\pi f \delta\tau_{\boldsymbol{a}}(u)}\, e^{j2\pi f_c \delta\tau_{\boldsymbol{a}}(u)} df du\,. \tag{32}$$

It can be observed that the error term $\delta\tau_{\boldsymbol{a}}$ entails a residual range migration as well as a residual Doppler migration, represented by the two exponential terms in the integral. Concerning the residual range migration, it is worth to point out that only scatterers quite far from the fulcrum undergo a tangible variation of the range position using $\tilde{\tau}_{\boldsymbol{a}}$ in lieu of $\tau_{\boldsymbol{a}}$. Because of the limited size of the targets of interest and the coarse range resolutions achievable with opportunistic signals (moreover worsened by the bistatic geometry), the residual range migrations due to $\delta\boldsymbol{\omega}$ can be neglected and (32) simplifies to

$$\widetilde{\boldsymbol{\mathcal{I}}}(x, y; \bar{z}) \approx \int_{-\frac{B}{2}}^{+\frac{B}{2}} S(f)\, df \int_{-\frac{T_a}{2}}^{+\frac{T_a}{2}} e^{j2\pi f_c\left(\delta\dot{\tau}_{\boldsymbol{a}} u + \delta\ddot{\tau}_{\boldsymbol{a}} \frac{u^2}{2}\right)} du. \tag{33}$$

The PSF of the image $\widetilde{\boldsymbol{\mathcal{I}}}$ can be derived by injecting the Doppler migration term in the GAF evaluation, carrying to (34), shown at the bottom of this page, where $m(\dot{\tau}_{\boldsymbol{a}}, \delta\dot{\tau}_{\boldsymbol{a}}; \delta\ddot{\tau}_{\boldsymbol{a}})$ denotes the solution of the integral over the slow time. With respect to the ideal solution in (9) [i.e., $m = \mathrm{sinc}(T_a f_c \dot{\tau}_{\boldsymbol{a}})$] and in case of motion estimation error, this comprises a Doppler shift ($\delta\dot{\tau}_{\boldsymbol{a}}$) and a defocusing term ($\delta\ddot{\tau}_{\boldsymbol{a}}$). The effects of the two terms are analyzed in the following sections.

1) Doppler Shift: Let us assume first that the defocusing effect can be neglected (i.e., $\delta\ddot{\tau}_{\boldsymbol{a}} \approx 0$). Under this condition, $m(*)$ in (34) takes the form $\mathrm{sinc}[T_a f_c(\dot{\tau}_{\boldsymbol{a}} + \delta\dot{\tau}_{\boldsymbol{a}})]$. To have a representation of this PSF in spatial coordinates, we can write $\delta\dot{\tau}_{\boldsymbol{a}}$ as in (13) by replacing $\boldsymbol{M}_\omega$ with $\boldsymbol{M}_{\delta\omega}$. That is, by replacing the actual instantaneous angular velocity with their error versions, we obtain

$$\begin{aligned}\delta\dot{\tau}_{\boldsymbol{a}} &= -\frac{2\cos\left(\beta/2\right)}{c}\left(\delta\boldsymbol{\omega}^0 \times \hat{\boldsymbol{\phi}}_\beta\right)^T \boldsymbol{a} \\ &= -\frac{2\cos\left(\beta/2\right)}{c}\|\delta\boldsymbol{\omega}^0\|\sin(\delta\zeta)\,\widehat{\delta\boldsymbol{\xi}}^T\boldsymbol{a} \\ &= -\frac{\delta\omega_{\mathrm{Eff}}}{c}\widehat{\delta\boldsymbol{\xi}}^T\boldsymbol{a}\end{aligned} \tag{35}$$

where $\delta\zeta$ is the angle between $\delta\boldsymbol{\omega}^0$ and $\hat{\boldsymbol{\phi}}_\beta$, $\widehat{\delta\boldsymbol{\xi}}$ is the unit vector normal to the plane containing $\delta\boldsymbol{\omega}^0$ and $\hat{\boldsymbol{\phi}}_\beta$, and $\delta\omega_{\mathrm{Eff}}$ is defined as $2\cos(\beta/2)\|\delta\boldsymbol{\omega}^0\|\sin(\delta\zeta)$. Therefore, omitting the initial phase term, the image PSF can be rewritten as (36), shown at the bottom of this page, where $\tilde{\omega}_{\mathrm{Eff}}\,\widetilde{\hat{\boldsymbol{\xi}}} = \omega_{\mathrm{Eff}}\,\hat{\boldsymbol{\xi}} + \delta\omega_{\mathrm{Eff}}\widehat{\delta\boldsymbol{\xi}}$. Comparing $\tilde{\chi}(\boldsymbol{a})$

$$\tilde{\chi}(\boldsymbol{a}) \approx e^{j2\pi f_c \tau_{\boldsymbol{a}}^0} \int_{-\frac{B}{2}}^{+\frac{B}{2}} \bar{P}(f)\, e^{j2\pi f \tau_{\boldsymbol{a}}^0} df \times \int_{-\frac{T_a}{2}}^{+\frac{T_a}{2}} e^{j2\pi f_c \dot{\tau}_{\boldsymbol{a}} u} e^{j2\pi f_c \delta\dot{\tau}_{\boldsymbol{a}} u} e^{j\pi f_c \delta\ddot{\tau}_{\boldsymbol{a}} u^2} du = e^{j2\pi f_c \tau_{\boldsymbol{a}}^0}\, p\left(\tau_{\boldsymbol{a}}^0\right)\ m(\dot{\tau}_{\boldsymbol{a}}, \delta\dot{\tau}_{\boldsymbol{a}}; \delta\ddot{\tau}_{\boldsymbol{a}})\,. \tag{34}$$

with the ideal PSF (17), we can observe that the error term $\delta\boldsymbol{\omega}^0$ implies an apparent azimuth resolution direction equal to $\widetilde{\hat{\boldsymbol{\xi}}}$ in lieu of $\hat{\boldsymbol{\xi}}$, while the parameter defining the azimuth resolution value ω_{Eff} becomes $\tilde{\omega}_{\text{Eff}}$. Therefore, the apparent azimuth resolution direction in the image is given by $\tilde{\alpha}_\xi$, denoting the projection of $\widetilde{\hat{\boldsymbol{\xi}}}$ on the ground plane, while the image azimuth resolution (23) is modified into its apparent version

$$\tilde{\rho}_{\tilde{\alpha}_\xi} = \frac{0.886}{\cos\left(\tilde{\psi}_\xi\right)} \frac{\lambda}{\tilde{\omega}_{\text{Eff}} T_a} \tag{37}$$

where $\tilde{\psi}_\xi$ is the angle between $\widetilde{\hat{\boldsymbol{\xi}}}$ and the ground plane. Then, by means of (36), the resulting resolution cell of the image $\tilde{\boldsymbol{\mathcal{I}}}$ can be calculated by resorting to the resolution ellipse as done in (24), looking for the locus of points for which $\tilde{\chi}(\boldsymbol{a}) = 1/\sqrt{2}$. This provides the apparent versions of the best and worst spatial resolutions of the image $\tilde{\rho}_{\text{min}}$ and $\tilde{\rho}_{\text{MAX}}$ with directions $\tilde{\alpha}_{\text{min}}$ and $\tilde{\alpha}_{\text{MAX}}$, respectively. Therefore, on the ground plane, $\tilde{\chi}(\boldsymbol{a})$ at first order can be regarded as a scaled and rotated version of $\chi(\boldsymbol{a})$.

Note that the estimation task must provide both an orientation and a magnitude of the rotation vector, namely, it must provide estimation for both $\hat{\boldsymbol{\xi}}$ and ω_{Eff}. However, in some scenarios, the orientation of the rotation vector could be known in advance, for example, if the target is forced to rotate around a specific direction, for example in the case of a ship observed in low sea state conditions where pitch and roll could be neglected. Therefore, we can consider the possible situations: 1) $\widetilde{\hat{\boldsymbol{\xi}}} = \hat{\boldsymbol{\xi}}$ and 2) $\widetilde{\hat{\boldsymbol{\xi}}} \neq \hat{\boldsymbol{\xi}}$. The former case occurs when the error on the constant part of the rotation vector is confined to the magnitude; therefore, the estimated version of the rotation vector can be written as $\tilde{\boldsymbol{\omega}}^0 = \boldsymbol{\omega}^0/\epsilon_\omega$ with $\epsilon_\omega > 0$.

A simple case study is here presented to illustrate the shape of the ideal and apparent PSFs. With reference to the passive ISAR geometry in Fig. 1, let us assume a passive receiver with $\theta^0_{Rx} = 0^\circ$ and $\psi^0_{Tx} = 0^\circ$ collecting the signal emitted by one transponder of a DVB-S transmitter of opportunity with bandwidth 32 MHz and carrier frequency 11.347 GHz and reflected by a rotating target characterized by rotation vector $\boldsymbol{\omega} = \boldsymbol{\omega}^0 = [-0.3 \quad 0 \quad 2]^T$ °/s. The transmitter illuminates the target with aspect and elevation angles $\theta^0_{Tx} = 45^\circ$ and $\psi^0_{Tx} = 37^\circ$, respectively, thus resulting in a bistatic angle $\beta = 55.62^\circ$. The aperture time is set equal to 0.5 s and, for the sake of simplicity, a constant power density of the DVB-S signal is assumed over the receiver bandwidth (i.e., $p(*)$ takes the form of a sinc function). Fig. 3 shows the resulting PSFs and the corresponding resolution ellipses considering the following estimates of the rotation vector:

1) $\tilde{\boldsymbol{\omega}} = \boldsymbol{\omega}$, i.e., ideal case $\chi(\boldsymbol{a})$ [see Fig. 3(a)];
2) $\tilde{\boldsymbol{\omega}} = [-0.39 \quad 0 \quad 2.6]^T$ °/s, i.e., $\tilde{\boldsymbol{\omega}} = 1.3\,\boldsymbol{\omega}$, and therefore, $\tilde{\chi}(\boldsymbol{a})$ when $\tilde{\omega}_{\text{Eff}} \neq \omega_{\text{Eff}}$ but $\widetilde{\hat{\boldsymbol{\xi}}} = \hat{\boldsymbol{\xi}}$ [see Fig. 3(b)];
3) $\tilde{\boldsymbol{\omega}} = [0 \quad -0.5 \quad 2.1]^T$ °/s, i.e., $\tilde{\chi}(\boldsymbol{a})$ when $\tilde{\omega}_{\text{Eff}} \neq \omega_{\text{Eff}}$ and $\widetilde{\hat{\boldsymbol{\xi}}} \neq \hat{\boldsymbol{\xi}}$ [see Fig. 3(c)].

Comparing the figures, it can be seen that in the case of motion error confined to the magnitude of the rotation vector, $\tilde{\chi}(\boldsymbol{a})$ essentially undergoes a shrinkage (if $\epsilon_\omega < 1$, as in the considered example) or expansion ($\epsilon_\omega > 1$) over the direction of the image azimuth resolution. In the case of motion estimation errors on both the magnitude and direction of the rotation vector, the nominal and apparent directions of the azimuth resolution directions differ and, as a consequence, $\tilde{\chi}(\boldsymbol{a})$ undergoes both a rotation and a scaling with respect to $\chi(\boldsymbol{a})$. In the considered example, the best spatial resolution direction α_{min} is equal to 108.8° in the ideal case $\chi(\boldsymbol{a})$ and it remains unaltered for $\tilde{\chi}(\boldsymbol{a})$ when $\widetilde{\hat{\boldsymbol{\xi}}} = \hat{\boldsymbol{\xi}}$; in contrast, for $\tilde{\chi}(\boldsymbol{a})$ when $\widetilde{\hat{\boldsymbol{\xi}}} \neq \hat{\boldsymbol{\xi}}$, $\tilde{\alpha}_{\text{min}} = 113.6^\circ$.

2) Defocusing: So far, we assumed a negligible quadratic phase term because of the motion estimation error. If such a condition does not apply, $m(\dot{\tau}_{\boldsymbol{a}}, \delta\dot{\tau}_{\boldsymbol{a}}; \delta\ddot{\tau}_{\boldsymbol{a}})$ takes the form of a blurred sinc function centered in $(\dot{\tau}_{\boldsymbol{a}} + \delta\dot{\tau}_{\boldsymbol{a}})$ with higher sidelobes level according to $\delta\ddot{\tau}_{\boldsymbol{a}}$. Criteria to avoid the kth scatterer being significantly defocused can be set by imposing that the uncompensated quadratic phase at the edge of the CPI (i.e., at $u = T_a/2$) is below a given angle φ_{lim} (depth of focus criterion), i.e., from (31) and (33)

$$\delta\varphi_k = \left| \pi \frac{T_a^2}{2} \frac{\cos\left(\frac{\beta}{2}\right)}{\lambda} \left(\hat{\boldsymbol{\phi}}_\beta^T \delta\boldsymbol{\Omega} + \left(\delta\dot{\boldsymbol{\omega}} \times \hat{\boldsymbol{\phi}}_\beta \right)^T \right) \boldsymbol{a}_k \right| \leq \varphi_{\text{lim}}. \tag{38}$$

In active high-resolution imaging systems, a widely adopted assumption is $\varphi_{\text{lim}} = 90^\circ$; however, this is somehow arbitrary, and the specific criterion can be set depending on the particular user requirements [28]. In the passive ISAR scenario, due to the challenging conditions and the lower expected image quality, this criterion might be relaxed allowing φ_{lim} greater than 90°. Some examples of image PSFs for different $\delta\varphi_k$ values are provided in the following.

Actually, for a given level of motion estimation errors, scatterers undergo more significant defocusing when the CPI is extended, especially in the case of uncompensated accelerations (i.e., $\delta\dot{\boldsymbol{\omega}} \neq 0$). As a case study, let us consider the geometry in Fig. 3 and assume $T_a = 0.8$ s, while the target rotation includes both a constant rotation vector $\boldsymbol{\omega}^0 = [-0.3 \quad 0 \quad 2]^T$ °/s and a rotation rate vector $\dot{\boldsymbol{\omega}} = [0.1 \quad -0.1 \quad 0.2]^T$ °/s^2. Let us also assume the estimation error equal to 10% of the actual value on the constant components ($\delta\boldsymbol{\omega}^0 = [-0.03 \quad 0 \quad 0.2]^T$ °/s) and an error equal to 30% on the linear components ($\delta\dot{\boldsymbol{\omega}} = [0.03 \quad -0.03 \quad 0.06]^T$ °/s^2). Fig. 4 shows the residual quadratic phase at the edge of the CPI as a function of the scatterer's coordinates (assuming them lying on the ground plane). As is apparent, for equal distance from the fulcrum, a different level of defocusing is experienced according to the scatterer's angular position.

$$\tilde{\chi}(\boldsymbol{a}) \approx p\left[2\cos\left(\frac{\beta}{2}\right)\hat{\boldsymbol{\phi}}_\beta^T \boldsymbol{a}\right] \text{sinc}\left[\frac{T_a}{\lambda}\left(\omega_{\text{Eff}}\hat{\boldsymbol{\xi}}^T\boldsymbol{a} + \delta\omega_{\text{Eff}}\widetilde{\delta\hat{\boldsymbol{\xi}}}^T\boldsymbol{a}\right)\right] = p\left[2\cos\left(\frac{\beta}{2}\right)\hat{\boldsymbol{\phi}}_\beta^T \boldsymbol{a}\right] \text{sinc}\left[\frac{T_a}{\lambda}\tilde{\omega}_{\text{Eff}}\widetilde{\hat{\boldsymbol{\xi}}}^T\boldsymbol{a}\right] \tag{36}$$

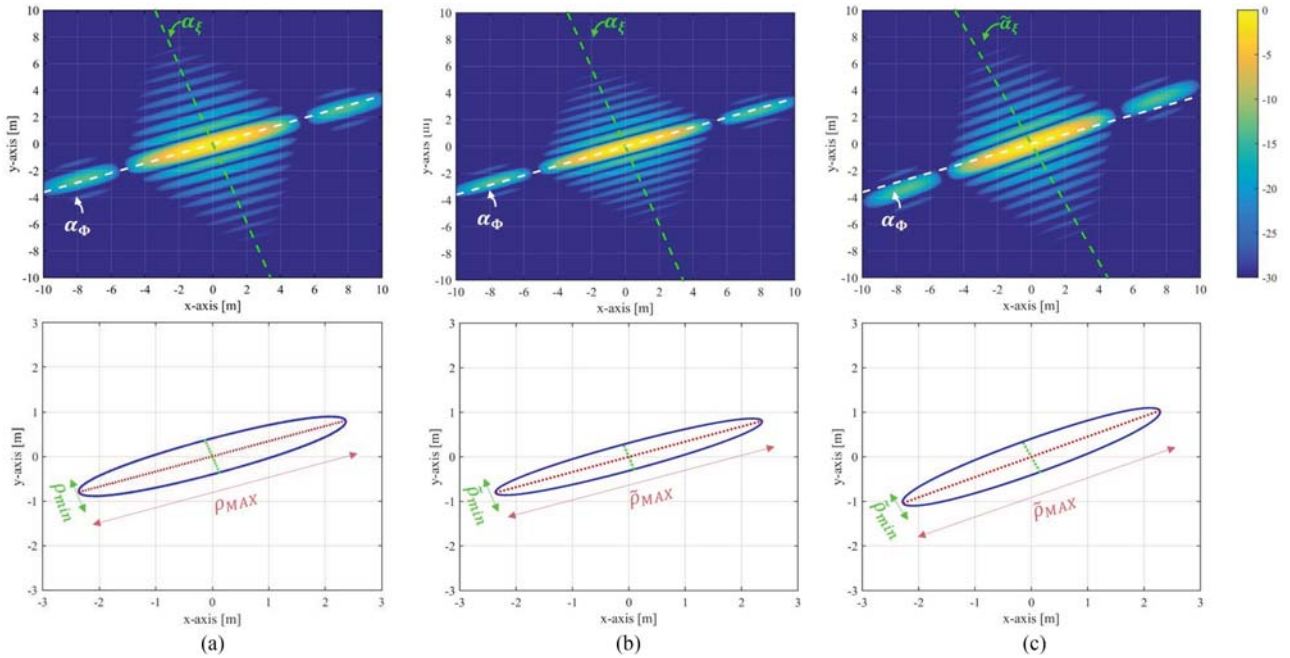

Fig. 3. Passive ISAR PSF examples in [dB] (top row) and corresponding resolution ellipses (bottom row). (a) Ideal focusing. (b) Estimation error confined to the magnitude of the rotation vector. (c) Estimation error in both magnitude and direction of the rotation vector.

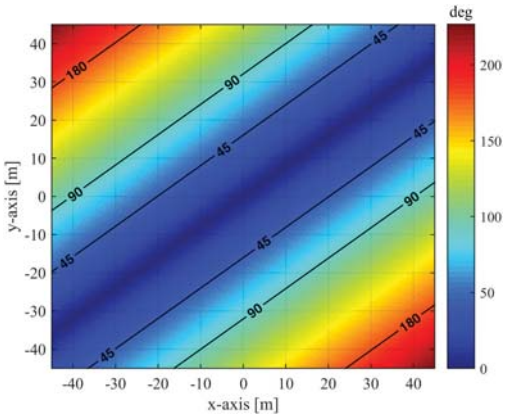

Fig. 4. Residual quadratic phase φ_k inside the target area.

To show the resulting PSFs when affected by different quadratic phase terms, BPA as in (32) has been implemented by simulating the returns from point scatterers in the following positions: (0, 0) m (i.e., target fulcrum), $\varphi_1 = 0°$; (-16, 19) m, $\varphi_2 \approx 90°$; and (-33, 38) m, $\varphi_3 \approx 180°$. Fig. 5 shows the resulting images (the figures have been centered around the scatterer position in the image $\widetilde{\boldsymbol{\mathcal{I}}}$: because of $\delta\boldsymbol{\omega}^0$, each scatterer will appear in a position different from the nominal one, as it will be addressed in the following section.) Comparing the images, it can be observed that the focusing quality progressively deteriorates, also causing a loss in SNR. A slight defocusing is observed for $\varphi_k \leq 90°$, a medium defocusing is experienced for $90° < \varphi_k \leq 180°$, while the focusing capability is severely compromised when $\varphi_k > 180°$.

B. Image Distortions

As shown in (34), rotation errors entail a Doppler shift and a defocusing term for each scatterer. While the latter affects the quality of the focusing, the former entails an erroneous scaling of the Doppler axis, thus causing mispositioning of target scatterers in the final image. The resulting image distortion negatively affects (geometrical) target size estimation, which is the main information typically used by passive ISAR users for classification procedures [29]. In this section, we derive closed-form equations to predict how the ideal scatterer position $\bar{\boldsymbol{a}}_k$ in $\boldsymbol{\mathcal{I}}$ is mapped into the "apparent" position $\widetilde{\bar{\boldsymbol{a}}}_k$ in image $\widetilde{\boldsymbol{\mathcal{I}}}$ because of errors on the rotation vector. Particularly, we derive a matrix transforming $\bar{\boldsymbol{a}}_k$ into $\widetilde{\bar{\boldsymbol{a}}}_k$ for a given observation geometry and motion estimation errors, referred to as deformation matrix.

In the general case, the estimation of the rotation vector implies an estimate of the azimuth resolution direction different from the nominal one, i.e., $\widetilde{\hat{\boldsymbol{\xi}}} \neq \hat{\boldsymbol{\xi}}$. To find the apparent position of the scatterer, we can consider that $\delta\boldsymbol{\omega}$ does not affect the range position of the scatterer, i.e., $\widetilde{\bar{\boldsymbol{a}}}_k$ and $\bar{\boldsymbol{a}}_k$ belong to the same isorange line. Moreover, the scatterer's nominal delay rate is equal to the delay rate calculated using the estimated version of the rotation vector and the apparent scatterer position. Combining these two constraints, the following linear system can be written:

$$\begin{cases} \hat{\boldsymbol{\phi}}_{\beta_{\setminus z}}^T \widetilde{\bar{\boldsymbol{a}}}_k = \hat{\boldsymbol{\phi}}_{\beta_{\setminus z}}^T \boldsymbol{P}\boldsymbol{a}_k \\ \tilde{\omega}_{\text{Eff}} \widetilde{\hat{\boldsymbol{\xi}}}_{\setminus z}^T \widetilde{\bar{\boldsymbol{a}}}_k = \omega_{\text{Eff}} \hat{\boldsymbol{\xi}}_{\setminus z}^T \boldsymbol{P}\boldsymbol{a}_k \end{cases}. \tag{39}$$

Therefore

$$\widetilde{\bar{\boldsymbol{a}}}_k = \begin{bmatrix} \hat{\boldsymbol{\phi}}_{\beta_{\setminus z}}^T \\ \widetilde{\hat{\boldsymbol{\xi}}}_{\setminus z}^T \end{bmatrix}^{-1} \begin{bmatrix} \hat{\boldsymbol{\phi}}_{\beta_{\setminus z}}^T \\ \frac{\omega_{\text{Eff}}}{\tilde{\omega}_{\text{Eff}}} \hat{\boldsymbol{\xi}}_{\setminus z}^T \end{bmatrix} \bar{\boldsymbol{a}}_k = \boldsymbol{S}_{\tilde{\xi}} \bar{\boldsymbol{a}}_k \tag{40}$$

where $\boldsymbol{S}_{\tilde{\xi}}$ is the deformation matrix mapping the scatterer with ideal position $\bar{\boldsymbol{a}}_k$ in the image plane in its apparent position $\widetilde{\bar{\boldsymbol{a}}}_k$.

As explained in Section III-A, when $\boldsymbol{\omega}^0$ estimation error is confined to the magnitude of the rotation vector (i.e., $\tilde{\boldsymbol{\omega}}^0 =$

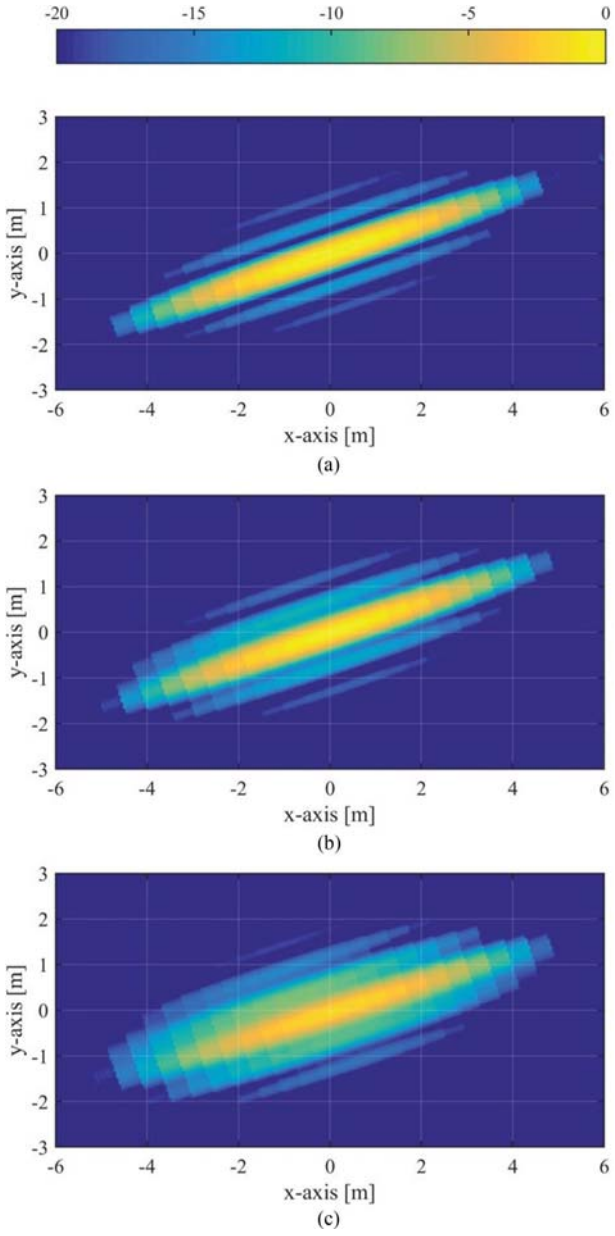

Fig. 5. PSF defocusing. (a) No defocusing ($\varphi_k = 0°$). (b) Medium defocusing ($\varphi_k \approx 90°$). (c) Severe defocusing ($\varphi_k \approx 180°$).

$\boldsymbol{\omega}^0/\epsilon_\omega$), the nominal and apparent azimuth resolution directions coincide, i.e., $\widetilde{\hat{\boldsymbol{\xi}}} = \hat{\boldsymbol{\xi}}$. Let $\boldsymbol{S}_\xi$ be the deformation matrix pertaining this case, it can be obtained from (40) by replacing $\widetilde{\hat{\boldsymbol{\xi}}}_{\setminus z}$ with $\hat{\boldsymbol{\xi}}_{\setminus z}$ and $\omega_{\text{Eff}}/\tilde{\omega}_{\text{Eff}} = \epsilon_\omega$. After some calculus (see Appendix B), this carries to

$$\boldsymbol{S}_\xi = \frac{\begin{bmatrix} \text{tg}\,(\alpha_\xi) - \epsilon_\omega \text{tg}\,(\alpha_\Theta) & \text{tg}\,(\alpha_\Theta)\,\text{tg}\,(\alpha_\xi)\,(1-\epsilon_\omega) \\ \epsilon_\omega - 1 & \epsilon_\omega \text{tg}\,(\alpha_\xi) - \text{tg}\,(\alpha_\Theta) \end{bmatrix}}{\text{tg}\,(\alpha_\xi) - \text{tg}\,(\alpha_\Theta)}. \tag{41}$$

From the deformation matrix in (40), as well as its special form (41), the kth scatterer position error can be calculated as the distance between the nominal and apparent scatterer positions, i.e.,

$$\delta\bar{\boldsymbol{a}}_k = \left(\widetilde{\bar{\boldsymbol{a}}}_k - \bar{\boldsymbol{a}}_k\right) = \left(\boldsymbol{S}_{\tilde{\xi}} - \boldsymbol{I}\right) \bar{\boldsymbol{a}}_k \tag{42}$$

where $\boldsymbol{I}$ is the 2×2 identity matrix.

As a case study, let us consider the same scenario in Fig. 3 and a target composed of nine point-like scatterers distributed in $\mathbb{R}^3$ as follows: $\boldsymbol{a}_1 = [0,0,0]^T$ m (i.e., target fulcrum), $\boldsymbol{a}_2 = [-25,-25,0]^T$ m, $\boldsymbol{a}_3 = [-25,25,0]^T$ m, $\boldsymbol{a}_4 = [25,-25,0]^T$ m, $\boldsymbol{a}_5 = [25,25,0]^T$ m, $\boldsymbol{a}_6 = [-15,0,15]^T$ m, $\boldsymbol{a}_7 = [15,0,15]^T$ m, $\boldsymbol{a}_8 = [0,-15,15]^T$ m, and $\boldsymbol{a}_9 = [0,15,15]^T$ m. Fig. 6(a) shows the image $\boldsymbol{\mathcal{I}}$ focused via BPA using nominal rotation vector [PSF in Fig. 3(a)], where the green markers denote the nominal scatterers' positions on the ground plane $\bar{\boldsymbol{a}}_k$ evaluated by (9). Then, BPA focusing is implemented injecting an estimation error such that $\tilde{\boldsymbol{\omega}} = 1.3\ \boldsymbol{\omega}$ [PSF in Fig. 3(b)], and the corresponding image is shown in Fig. 6(b), where the red markers denote the theoretical apparent positions evaluated by the deformation matrix $\boldsymbol{S}_\xi$ in (41). As it is apparent, the positions of the scatterers in the image correspond to the theoretical expectations. Finally, Fig. 6(c) shows the result of the BPA focusing using $\tilde{\boldsymbol{\omega}} = [0 \quad -0.5 \quad 2.1\ ]^T$ °/s [PSF in Fig. 3(c)]. In this case, as $\widetilde{\hat{\boldsymbol{\xi}}} \neq \hat{\boldsymbol{\xi}}$, the theoretical apparent scatterer positions have been calculated using the general form $\boldsymbol{S}_{\tilde{\xi}}$ of the deformation matrix (40). Also in this case the correspondence between scatterers position in $\widetilde{\boldsymbol{\mathcal{I}}}$ and theoretical expectations is achieved.

It is worth mentioning that a further simplification of the deformation matrix in (41) can be done when the ground plane and the IPP coincide. This situation occurs when the bistatic range resolution direction lies on the ground plane and the rotation vector is collinear to the vertical axis z, as for example in the case of DVB-T-based passive radar located on the ground observing a ship undergoing a dominant yaw motion. As in such a case range and azimuth resolutions are orthogonal over the image, $\boldsymbol{S}_\xi$ can be simplified as

$$\boldsymbol{S}_\xi^\perp = \boldsymbol{M}_{\alpha_\xi}^T\, \boldsymbol{Q} \boldsymbol{M}_{\alpha_\xi} \tag{43}$$

where the apex $\perp$ denotes the case $\alpha_\xi = \alpha_\Theta + 90°$, $\boldsymbol{M}_{\alpha_\xi}$ is the 2-D clockwise rotation matrix by angle α_ξ, and $\boldsymbol{Q} = \text{diag}\{[\epsilon_\omega, 1]\}$ is a scaling matrix. Namely, in these particular conditions, the apparent scatterer position can be calculated from the nominal one by applying: 1) a clockwise rotation by angle α_ξ, allowing to transit in a reference plane (x', y'), where x' and y' represent the azimuth and range resolution directions; 2) a scaling over x' according to the ratio between the nominal and estimated value of the target speed, i.e., ϵ_ω; 3) a counterclockwise rotation by angle α_ξ to return in the (x, y) reference system. Moreover, the magnitude of the position error (42) can be written as

$$\|\delta\bar{\boldsymbol{a}}_k^\perp\| = |\epsilon_\omega - 1|\ \ |\cos\left(\alpha_\xi - \alpha_k\right)|\, \|\bar{\boldsymbol{a}}_k\| \tag{44}$$

where α_k is the angular position of the scatterer on the ground plane (measured counterclockwise from the x-axis). Therefore, for the ground plane coinciding with the IPP and for equal distance from the fulcrum, the position error is maximum (in

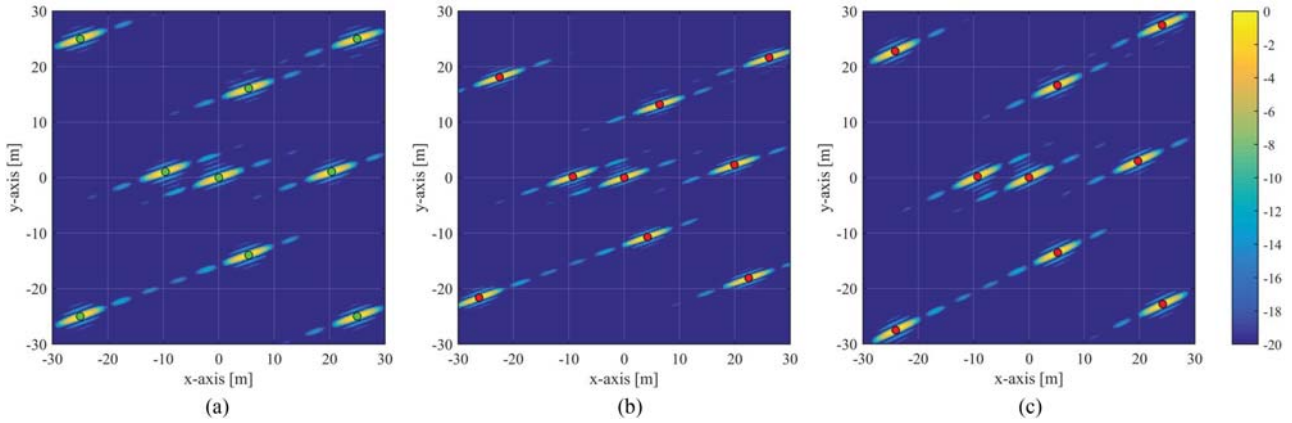

Fig. 6. Simulated BPA images (in [dB] and normalized in amplitude to their peak values) and theoretical scatterers positions (a) focusing with nominal target motion, (b) focusing in the case $\tilde{\omega}_{\text{Eff}} \neq \omega_{\text{Eff}}$ but $\widetilde{\hat{\boldsymbol{\xi}}} = \hat{\boldsymbol{\xi}}$, and (c) focusing for $\tilde{\omega}_{\text{Eff}} \neq \omega_{\text{Eff}}$ and $\widetilde{\hat{\boldsymbol{\xi}}} \neq \hat{\boldsymbol{\xi}}$.

magnitude) for scatterers aligned in the azimuth resolution direction (i.e., $\alpha_k = \alpha_\xi$) and it is zero for scatterers lying on the range resolution direction (i.e., $\alpha_k = \alpha_\Theta$). The derivations of (43) and (44) are reported in Appendix C.

IV. Numerical Analysis

In this section, we provide numerical analyses to investigate the robustness of the BPA-based passive ISAR focusing on different scenarios. A few possible user requirements of image quality are preliminarily defined, in order to establish a required accuracy level for the target motion estimation module. Particularly, five criteria are here defined to measure the impact of the motion estimation error in the image area, from level 0 (negligible) to level 4 (severe).

Motion estimation errors are assumed negligible if they cause residual quadratic phase errors below $\varphi_{\text{lim}} = 45°$ and if the maximum shift of the scatterer is lower than the best spatial resolution of the system ρ_{min}. However, such constraints can be particularly demanding for passive ISAR systems. A scatterer can be sufficiently well-focused as long as the quadratic phase errors entail a residual phase below 90° [see Fig. 5(b)]. Moreover, it is worth to point out that the exploitation of signals of opportunity makes the resolution cell generally much larger along α_{MAX} than along α_{min}, and therefore, the condition on the maximum shift could further be relaxed. Indeed, especially in scenarios characterized by coarse spatial resolutions [30], a less stringent requirement could be set by imposing that the maximum shift cannot exceed the equivalent diameter ρ_{eq}, defined as the diameter of the circle having the same area as the resolution ellipse, i.e., $\rho_{\text{eq}} = \sqrt{\rho_{\text{min}}\rho_{\text{MAX}}}$. Based on the considerations above, we can define two criteria corresponding to negligible and slight impact.

1) Level 0—negligible impact: The position error is below the best spatial resolution of the image ρ_{min} and the quadratic phase error does not exceed 45°. Under such conditions, $\boldsymbol{\mathcal{J}}$ is very close to $\widetilde{\boldsymbol{\mathcal{J}}}$, and therefore, no appreciable effects on the information contained in the image are expected.
2) Level 1—slight impact: The shift is greater than ρ_{min} but it does not exceed ρ_{eq} and the quadratic phase error does not exceed 90°. Setting $\varphi_{\text{lim}} = 90°$ guarantees a still good quality of the focusing; moreover, a shift lower than ρ_{eq} is supposed only slightly affecting the classifier performance. Under such conditions, some differences between $\boldsymbol{\mathcal{J}}$ and $\widetilde{\boldsymbol{\mathcal{J}}}$ can be observed, but these are supposed to do not sensibly affect the classifier performance.

For shifts larger than ρ_{eq} and/or residual quadratic phase errors larger than 90°, some significant differences between $\boldsymbol{\mathcal{J}}$ and $\widetilde{\boldsymbol{\mathcal{J}}}$ begin to appear that could bring the classifier to commit errors. Particularly, three further criteria for a higher impact of the errors can be defined.

1) Level 2—medium impact: The shift is still lower than ρ_{eq}, but the quality of the focusing deteriorates being the quadratic phase error larger than 90° but still below 180°. Even though the geometrical distortion is tolerable, SNR losses due to defocusing could partly compromise the capability of correctly extracting the target segment from the background.
2) Level 3—high impact: φ_{lim} is set equal to 180° and the position error is larger than ρ_{eq}, but still lower than the worst spatial resolution of the system ρ_{MAX}. Under these conditions, geometric distortion is supposed to become relevant.
3) Level 4—severe impact: If the quadratic phase error exceeds 180° and/or the position error is larger than ρ_{MAX}, the reliability of the information contained in the focused image is assumed severely affected, possibly compromising the success of the classification procedure.

For the sake of clarity, Table I summarizes these criteria. It is worth to stress that these are used here as an example, as they depend on the particular classifier behavior and settings. Different requirements could be obviously adopted still maintaining the quality of the results discussed in the remainder of the section.

First, let us consider a passive radar system exploiting DVB-T signals, using a single channel with a bandwidth of 7.61 MHz and carrier frequency of 626 MHz [2], [20]. The system geometry is given by transmitter and receiver coplanar with the target and characterized by the angles $\theta_T^0 = 45° + \frac{\beta}{2}$, $\theta_R^0 = 45° - \frac{\beta}{2}$, and $\psi_T^0 = \psi_R^0 = 0°$. During the aperture time equal to 2.5 s, the target is supposed to constantly yaw at the speed of 2 °/s. In the

TABLE I
ADOPTED USER REQUIREMENTS

Impact of motion errors	Criteria*
Level 0 – Negligible	$\boldsymbol{a}_k$: $\varphi_k \leq 45° \wedge \|\|\delta\overline{\boldsymbol{a}}_k\|\| \leq \rho_{\min}$
Level 1 – Slight	$\boldsymbol{a}_k$: $\varphi_k \leq 90° \wedge \rho_{\min} < \|\|\delta\overline{\boldsymbol{a}}_k\|\| \leq \rho_{\text{eq}}$
Level 2 – Medium	$\boldsymbol{a}_k$: $90° < \varphi_k \leq 180° \wedge \|\|\delta\overline{\boldsymbol{a}}_k\|\| \leq \rho_{\text{eq}}$
Level 3 – High	$\boldsymbol{a}_k$: $\varphi_k < 180° \wedge \rho_{\text{eq}} < \|\|\delta\overline{\boldsymbol{a}}_k\|\| \leq \rho_{\text{MAX}}$
Level 4 – Severe	$\boldsymbol{a}_k$: $\varphi_k < 180° \vee \|\|\delta\overline{\boldsymbol{a}}_k\|\| > \rho_{\text{MAX}}$

* $\wedge$: AND; $\vee$: AND/OR

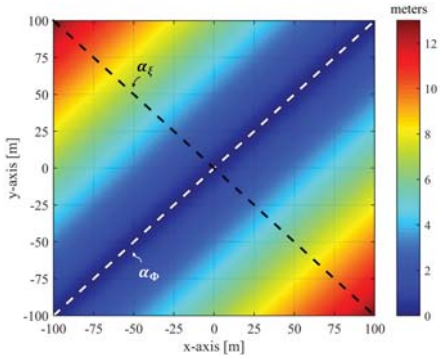

Fig. 7. DVB-T passive radar case study – position error $\|\delta\overline{\boldsymbol{a}}_k^{\perp}\|$.

following, we assume the exact knowledge of the direction of the rotation vector and consider the yaw speed estimated with different error levels, in the form of $\delta\omega_z$ equal to a percentage of the absolute velocity (i.e., $\tilde{\boldsymbol{\omega}}^0 = \epsilon_\omega \boldsymbol{\omega}^0$ case).

Fig. 7 shows the norm of the position error $\delta\overline{\boldsymbol{a}}_k$ as a function of the nominal scatterers coordinates over an area of 200 m $\times$ 200 m, which is supposed to be large enough to contain any target of practical interest in the considered scenario, when $\delta\omega_z = 10\%\omega_z$ (i.e., $\epsilon_\omega = 1.1$). We point out that in this case study, the ground plane coincides with the IPP, and therefore, the position error can be evaluated by means of (44). As expected, the position error is null for points lying in the range resolution direction α_Θ (white dotted line in the figure) while it maximizes over the azimuth resolution direction α_ξ (black dotted line).

The maximum allowed area can be defined as the region of the (x, y) plane containing the nominal scatterers' positions for which the impact of $\delta\omega_z$ does not exceed one of the criteria defined above. Since both resolution cell size and residual quadratic phase $\delta\varphi_k$ vary with the bistatic angle, we consider two bistatic geometries corresponding to bistatic angles $\beta_1 = 30°$ and $\beta_2 = 100°$. In the former case, the PSF is characterized by $\rho_{\min 1} = 2.52$ m and $\rho_{\text{MAX}1} = 18.08$ m, and therefore, $\rho_{\text{eq}_1} = 6.75$ m, while in the latter $\rho_{\min 2} = 3.78$ m and $\rho_{\text{MAX}2} = 27.17$ m, and therefore, $\rho_{\text{eq}_2} = 10.15$ m. The maximum allowed area is here calculated for both the geometries for different motion estimation errors, by considering $\delta\omega_z = (\epsilon_\omega - 1)\ \omega_z$ with $(\epsilon_\omega - 1) = 5\%,\ 10\%,\ 15\%,\ 30\%$. Fig. 8(a) and (b) shows the allowed areas experiencing negligible impact (level-0) for bistatic angles β_1 and β_2, respectively, while Fig. 8(c) and (d) shows the allowed areas for slight impact (level-1). Comparing Fig. 8(a) and (b) with Fig. 8(c) and (d), we can observe that, in parity of error percentage, targets belonging to greater dimensional classes can be imaged if the classifier can reliably operate under criteria level-1. However, a general tolerance of the focusing is observed even for the most stringent requirements (level 0), allowing an almost ideal focusing for quite inaccurate rotation motion estimations for target sizes of practical interest. It is worth to point out that in the considered scenario of constant rotation speed, the main effect of the motion estimation errors is the geometrical distortion of the resulting image. Noticeably, such a distortion does not depend on the absolute value of the rotation speed, but only on the relative error $\omega_{\text{Eff}}/\tilde{\omega}_{\text{Eff}}$ and, if $\widetilde{\hat{\boldsymbol{\xi}}} \neq \hat{\boldsymbol{\xi}}$, on the difference between the nominal and estimated azimuth resolution directions. Moreover, the scatterer position error is not a function of the bistatic angle: the differences among results for bistatic angles β_1 and β_2 in Fig. 8 are due to the different resolutions experienced, as both range and azimuth resolution are scaled by $\cos(\beta/2)$ with respect to their monostatic versions.

In the previous case study, the target was supposed to undergo a rotational motion confined to the plane around its vertical axis. However, in most cases, the target exhibits complex dynamics including pitch and roll rotations. Often, especially in the case of ships, these are modeled as sinusoidal rotations: the angles swept with time around the γth axis ($\gamma = x, y$) are given by $\vartheta_\gamma(u) = A_\gamma \sin(2\pi f_\gamma u + \varphi_\gamma)$, where A_γ, f_γ, and φ_γ are the amplitude, frequency, and initial phase of the sinusoidal motion [31]. In such conditions, the pitch and roll rotations exhibit both a constant and a time-varying component, equal to $\omega_\gamma^0 = A_\gamma 2\pi f_\gamma \cos(\varphi_\gamma)$ and $\dot{\omega}_\gamma = -A_\gamma (2\pi f_\gamma)^2 \sin(\varphi_\gamma)$, respectively. The recovery of the target 3-D rotation vector (besides time-varying) is a very challenging task even for dedicated active radar imaging systems, typically requiring high-range resolution, high SNR, and multichannel (colocated or distributed) receiver configurations [32], [33], [34], [35], [36]. When exploiting illuminators of opportunity, this goal might become extremely difficult, and often horizontal rotations (i.e., due to pitch and roll) are neglected in the focusing procedures. The methods presented in the article are exploited to investigate the tolerance of the BPA focusing when the presence of pitch and roll rotations is neglected. Particularly, we assume a ship target undergoing a dominant yaw motion with constant speed and additional sinusoidal pitch and roll rotations. The motion estimation module is supposed to be able to recover exactly the yaw motion while roll and pitch are completely neglected during the focusing. Namely, $\boldsymbol{\omega}(u) = [A_x \sin(2\pi f_x u + \varphi_x), A_y \sin(2\pi f_y u + \varphi_y),\ \omega_z^0]^T$ and $\delta\boldsymbol{\omega}(u) = [-A_x \sin(2\pi f_x u + \varphi_x), -A_y \sin(2\pi f_y u + \varphi_y), 0]^T$. To analyze the tolerance of the focusing for increasing pitch and roll, we fix the frequency and initial phase of the rotations and progressively increase their amplitude. Particularly, f_x and f_y have been set equal to 0.1 Hz, $\varphi_x = 30°$, and $\varphi_y = -45°$, while A_x and A_y have been set both equal to 0°, 0.5°, 1°, and 1.5° in four different case studies (A–D). Table II lists the target motion and the acquisition parameters. In this case study, we consider a DVB-S-based passive radar observing a ship target composed of many point-like scatterers with different levels of superstructure.

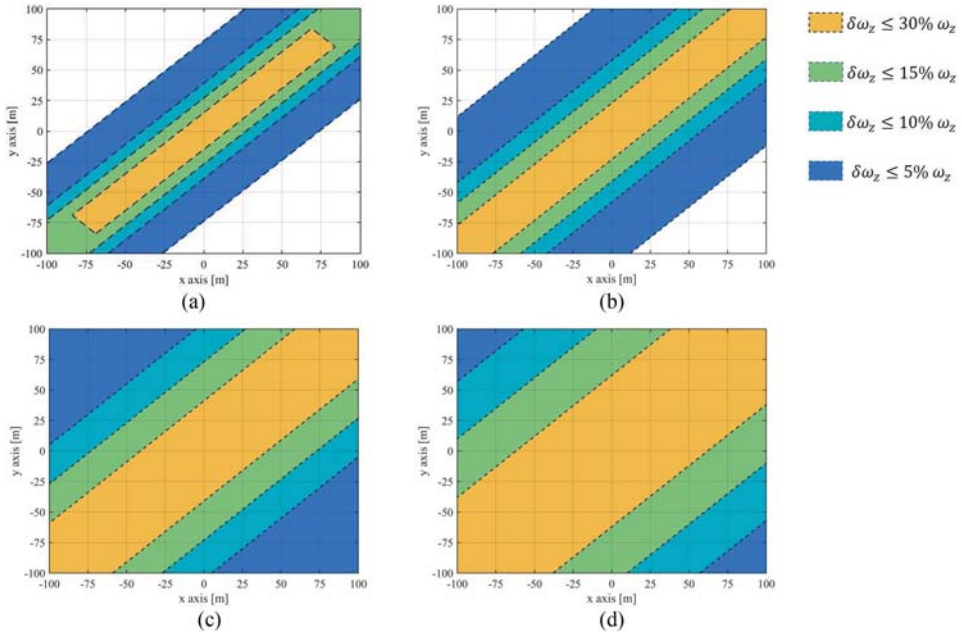

Fig. 8. DVB-T case, allowed target area for negligible focusing errors (a) $\beta = 30°$ and (b) $\beta = 100°$, and for slight focusing errors (c) $\beta = 30°$ and (d) $\beta = 100°$.

As DVB-S satellites operate in the Ku-band and transmit relatively wide bandwidths, in such a scenario passive ISAR products with good spatial resolution could be obtained, in principle enabling the extraction of finer details about the imaged target, in turn allowing more advanced classification procedures. To assess the tolerance of the BPA for different values of the roll and pitch rotations, for each case study, we assign different regions of $\mathbb{R}^3$ to one specific class following the user requirements defined in Table I.

Fig. 9 shows the achieved images for the four case studies A–D listed in Table II (corresponding to different levels of the sinusoidal roll and pitch amplitudes) along with the 3-D point scatterer target model. In these figures, each scatterer has been displayed with a marker according to the experienced level of impact of the motion estimation errors to highlight which parts of the target belong to the classes defined in Table I. Fig. 9(a) corresponds to null pitch and roll (case A), therefore, corresponding to the ideal image and serving as reference. When $A_x = A_y = 0.5°$ [case B, Fig. 9(b)], only scatterers quite close to the fulcrum experience almost no impact of the errors (blue "•" markers), but most of the target can be still imaged with a limited impact on the result (green "+" markers), and ship's endpoints only are affected by medium errors (magenta "×" markers). In fact, comparing the BPA image with the ideal result in Fig. 9(a), very limited differences can be observed. Increasing the amplitudes at 1° [case C, Fig. 9(c)], a general worsening of the image can be appreciated. In this case, most of the scatterers belonging to the ship deck are quite significantly shifted from their nominal positions (red "∗" markers) possibly affecting the capability of correctly extracting detailed information about the target shape. Moreover, as points outside the ground plane are the most sensitive to errors on the horizontal components of the rotation vector, the scatterers belonging to the mainmast are affected by a severe impact of neglecting pitch and roll (black "■" markers). Finally, when the amplitudes reach 1.5° [case D, Fig. 9(d)], most of the scatterers on the target edges are severely affected by the motion estimation errors. Comparing ISAR images in Fig. 9(a) and (d), it can be seen that, with respect to the ideal image, the target shape is much harder to recognize. The SNR losses caused by the defocusing makes the extraction of the individual scattering return from a noisy background difficult that, combined with the image distortion, reduce the match score with reference ship models [37], thus increasing the probability that a classifier assignes it to a different target type.

V. Experimental Results

A. DVB-T-Based Passive ISAR

Using passive radar systems based on digital terrestrial television illumination has been perhaps one of the first attempts to obtain images of man-made targets via passive ISAR approaches, being DVB-T the most adopted standard worldwide [2]. As these sources operate in the UHF/VHF-band, the resulting images may be characterized by a poor azimuth resolution that, when combined with the limited bandwidths (typically around 8 MHz), often results in low-resolution products. On the other hand, they can benefit from relatively large transmitted powers allowing them to achieve images characterized by significant SNRs. Moreover, by extending the CPI and adopting multichannels or compressive sensing-based approaches, the poor spatial resolution issue can be mitigated [3].

An experimental campaign has been conducted in order to collect DVB-T data in Livorno (Italy) using the experimental passive radar system ATLAS [see Fig. 10(a)], developed by Fraunhofer FHR. Such a system is a scalable software-defined

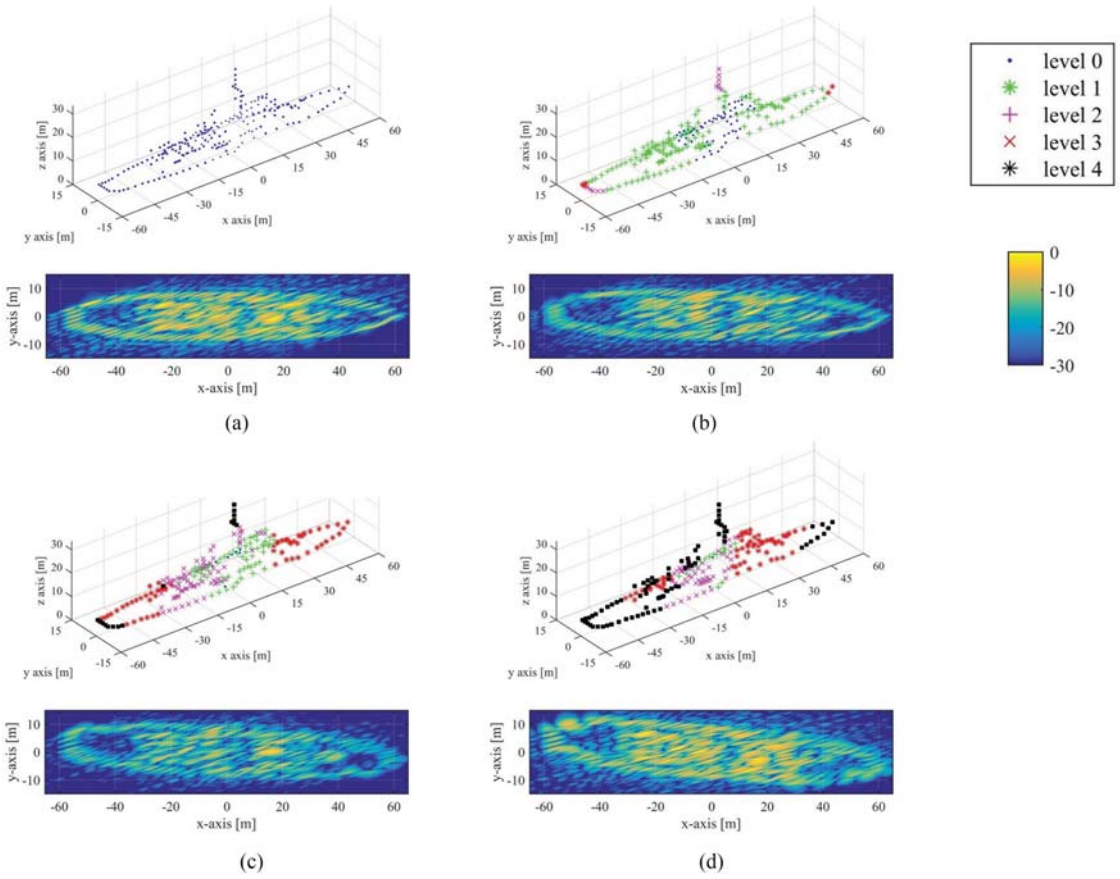

Fig. 9. DVB-S passive radar case study, BPA images, and 3-D target model for (a) case A (ideal focusing), (b) case B, (c) case C, and (d) case D.

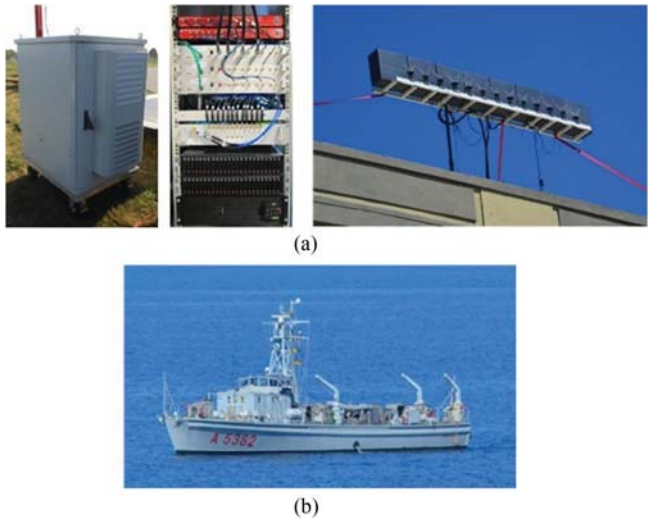

Fig. 10. DVB-T-based passive radar experimental campaign. (a) Receiving hardware. (b) Cooperative target side-view photograph.

radio-based passive radar for digital audio broadcasting /DVB-T, which consists of 12 RF receiving channels and is able to operate in the band from 470 to 870 MHz. For imaging purposes, here we consider only one of the 11 available surveillance channels, while the 12th channel is used to collect the reference signal. The exploited transmitter of opportunity was a DVB-T transmitter located at Monte Serra in Pisa (around 33 km northeast from the receiver) broadcasting a single DVB-T channel around the central frequency of 626 MHz. The military ship Porpora of length 32.4 m and width 6.4 m, shown in Fig. 10(b), was cruising predefined trajectories suited for ISAR imaging purposes at about 1500 m from the receiver and it was equipped with an inertial measurement unit (IMU) to record the target motion. Table III lists the parameters of the acquisition pertaining to a time interval of about 6 s which is used for imaging.

Fig. 11(a) shows the imaging result using the known-motion BPA. It can be observed that, due to the particular operative conditions, different scattering points along the x-axis, namely along the deck line, can be identified, while the size of the PSF along the y-axis is larger than the ferry's width. Therefore, the major information that can be extracted from this image is the length of the ferry. The black dotted line superimposed on the figure denotes the ship's centerline, whose edges have been highlighted with the black "•" markers, taken at a distance of 32 m (i.e., compliant with the ferry's nominal length). Then, two further images have been focused, using erroneous versions of the rotation vector, as described in the following.

As can be observed from Table III, the ferry was undergoing a dominant yaw motion. Particularly, the unit vector of $\boldsymbol{\omega}^0$

TABLE II
DVB-S-BASED PASSIVE ISAR CASE STUDY—SIMULATION PARAMETERS

Acquisition parameters			
Bandwidth		B	32 MHz
Carrier frequency		f_c	11.347 GHz
Tx aspect angle		θ_T^0	45 deg
Tx elevation angle		ψ_T^0	37 deg
Rx aspect angle		θ_R^0	0 deg
Rx elevation angle		ψ_R^0	0 deg
Bistatic angle		β	55.62 deg
Aperture time		T_a	0.5 s
Target motion model			
Roll	$\omega_x(u)$	$A_x \sin(2\pi f_x u + \varphi_x)$	
		$f_x = 0.1$ Hz, $\varphi_x = 30$ deg	
		Case A: $A_x = 0$ deg	
		$\omega_x^0 = 0$ deg/s	$\dot{\omega}_x = 0$ deg/s^2
		Case B: $A_x = 0.5$ deg	
		$\omega_x^0 = 0.27$ deg/s	$\dot{\omega}_x = -0.10$ deg/s^2
		Case C: $A_x = 1$ deg	
		$\omega_x^0 = 0.54$ deg/s	$\dot{\omega}_x = -0.20$ deg/s^2
		Case D: $A_x = 1.5$ deg	
		$\omega_x^0 = 0.82$ deg/s	$\dot{\omega}_x = -0.30$ deg/s^2
Pitch	$\omega_y(u)$	$A_y \sin(2\pi f_y u + \varphi_y)$	
		$f_y = 0.1$ Hz, $\varphi_y = -45$ deg	
		Case A: $A_x = 0$ deg	
		$\omega_y^0 = 0$ deg/s	$\dot{\omega}_y = 0$ deg/s^2
		Case B: $A_y = 0.5$ deg	
		$\omega_y^0 = 0.22$ deg/s	$\dot{\omega}_y = 0.14$ deg/s^2
		Case C: $A_y = 1$ deg	
		$\omega_y^0 = 0.44$ deg/s	$\dot{\omega}_y = 0.28$ deg/s^2
		Case D: $A_y = 1.5$ deg	
		$\omega_y^0 = 0.67$ deg/s	$\dot{\omega}_y = 0.42$ deg/s^2
Yaw	$\omega_z(u)$	$\omega_z^0 = 3$ deg/s	$\dot{\omega}_z = 0$ deg/s^2

TABLE III
DVB-T PASSIVE ISAR EXPERIMENTAL IMAGES PARAMETERS

Parameter		Value
Receiver bandwidth	B	8 MHz
Central frequency	f_c	626 MHz
Tx aspect angle	θ_T^0	142.81 deg
Tx elevation angle	ψ_T^0	29.73 deg
Rx aspect angle	θ_R^0	111.23 deg
Rx elevation angle	ψ_R^0	1.29 deg
Bistatic angle	β	41.35 deg
Aperture time	T_a	5900 ms
Ferry yaw speed	ω_z^0	-1.87 deg/s
Ferry pitch speed	ω_y^0	0.01 deg/s
Ferry roll speed	ω_x^0	-0.13 deg/s

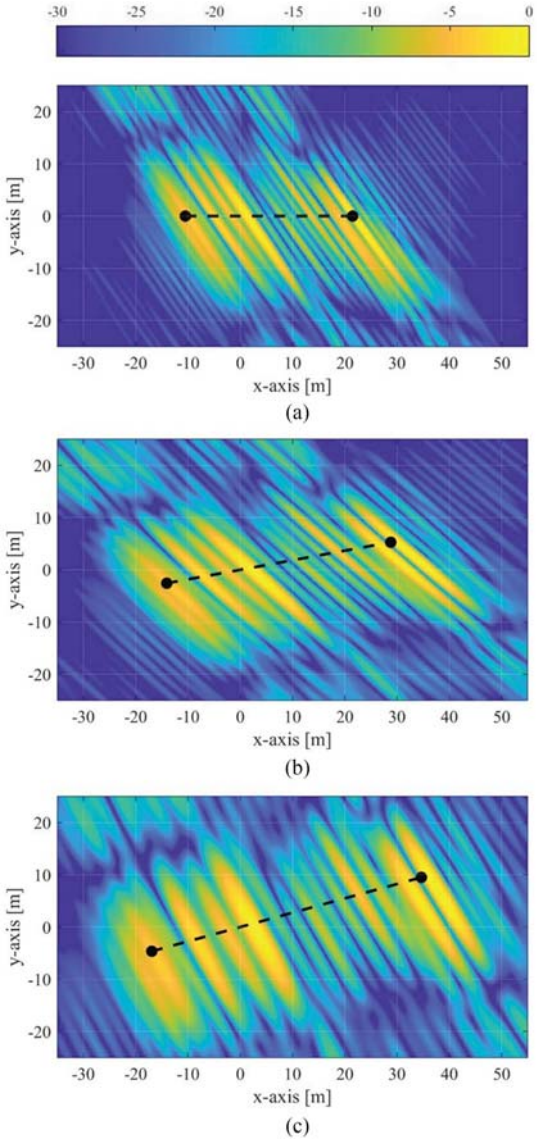

Fig. 11. DVB-T-based passive ISAR experimental images (in [dB] and normalized in amplitude to their peak values). (a) Focused image with IMU information. (b) Focused image with $\widetilde{\boldsymbol{\omega}}^0 = [-\sqrt{0.2} \;\; -\sqrt{0.2} \;\; -\sqrt{0.6}]^T$. (c) Focused image with $\widetilde{\boldsymbol{\omega}}^0 = [-\sqrt{0.25} \;\; -\sqrt{0.25} \;\; -\sqrt{0.5}]^T$.

is approximately equal to $[0 \;\; 0 \;\; -1]^T$, while its magnitude is about 1.87 °/s. In this case study, we assume a perfect knowledge of $\|\boldsymbol{\omega}^0\|$ and consider motion estimation errors confined to the direction of the rotation vector. Fig. 11(b) and (c) shows the resulting images focused using rotation vectors with directions $\widetilde{\boldsymbol{\omega}}^0 = [-\sqrt{0.2} \;\; -\sqrt{0.2} \;\; -\sqrt{0.6}\;]^T$ and $\widetilde{\boldsymbol{\omega}}^0 = [-\sqrt{0.25} \;\; -\sqrt{0.25} \;\; -\sqrt{0.5}\;]^T$, respectively. It could be shown that both images are affected by negligible defocusing ($\varphi_k < 45°$within the target area, (38)). However, a quite significant distortion is experienced. In the figures, the superimposed black "•" markers show the theoretical positions of the ferry's edges, (40), allowing us to appreciate as the individual scatterers are mapped into positions according to the theory. Therefore, the proposed theoretical framework allows error length estimation.

Specifically, identifying the ship's endpoints in the ISAR images and measuring the span over the x direction, in the nominal case a value very close to the actual one can be found, while about 45 m and 55 m are obtained from the ISAR images in Fig. 11(b) and (c), respectively, bringing to relative errors of about 40% and 70%.

B. DVB-S-Based Passive ISAR

The exploitation of DVB-S signals of opportunity is one of the most recent trends among the passive radar community, turning out in a promising solution for the protection of critical infrastructures, thanks to nearly global availability, relatively wide bands, and fine velocity resolutions [38], [39], [40]. DVB-S-based passive ISAR images can be characterized by fine spatial resolutions that could be even comparable to dedicated imaging systems, especially when signals emitted by multiple transponders are acquired. Indeed, the DVB-S spectrum is densely populated by multiple channels with little gaps, which can be combined to enhance the range resolution [8]. Moreover, signals with both horizontal and vertical polarization states are available, thus providing further degrees-of-freedom to enrich the image's information space [9], [19].

To obtain DVB-S-based passive ISAR data, experiments were conducted alongside the Rhine in Bonn, Germany. The experimental hardware was the passive radar system SABBIA developed by Fraunhofer FHR, as shown in Fig. 12(a). This comprised two identical receiver front-ends, one for surveillance and one for reference, both using a dish antenna with horizontal polarization. Each antenna was connected to a global positioning system/IMU to obtain precise information about location and antenna pointing direction, and they were both locked to the same 10 MHz reference signal to ensure phase coherence. The transmitter of opportunity was the Astra satellite 1KR located at the 19.2 °E orbital position, which provides coverage of all the European continent [41]. An instantaneous signal bandwidth of 80 MHz was acquired centered on the carrier frequency 11 347 MHz of the DVB-S spectrum. Fig. 12(b) shows the power spectral density measured by the reference channel, where it can be seen that slightly more than two transponders' emissions have been acquired. The target was the Königswinter ferry (46.24 m $\times$ 20 m), whose side-view photograph is shown in Fig. 12(c). The ferry was located at about 800 m from the receiver and it was equipped with an IMU located on its central superstructure [see Fig. 12(c)] to record its kinematics. In the trials, the target was observed for about 200 s, during which the target was rotating over a large angle, offering the chance to image it under different illumination and motion conditions.

The parameters of the first case study are listed in Table IV. In this case, to experimentally obtain a PSF of the image, the processed bandwidth was limited at 25 MHz around the central frequency 11361.75 MHz (i.e., +14.75 MHz from the acquired carrier) to process the signal pertaining to one single transponder, where the spectrum shows a nearly flat behavior [see Fig. 12(b)], and therefore, the corresponding range profile closely resembles a sinc function. However, as the DVB-S standard adopts a squared-root-raised cosine pulse shaping and, therefore, the spectrum is only approximately flat, a more complicated function than a sinc should be used to model the range response [42]. For the sake of convenience, here we do the approximation $p \approx \mathrm{sinc}(2B_{\mathrm{eq}} \cos(\frac{\beta}{2}) \hat{\boldsymbol{\phi}}_{\beta}^{T} \boldsymbol{a})$, where B_{eq} is the reciprocal of the time resolution evaluated at the – 4 dB level of the actual range response of the reference channel (here equal to ∼22 MHz).

We selected a short frame of about 200 ms in which an isolated strong return could be observed in the area corresponding to the central superstructure where the IMU was located. Particularly,

(a)

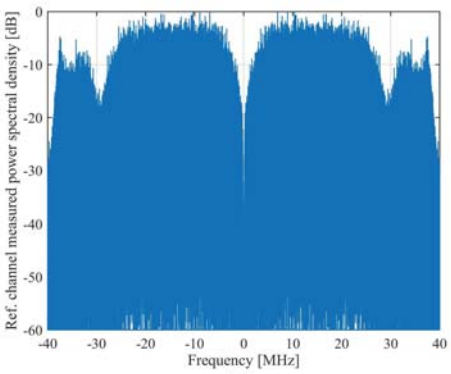

(b)

(c)

Fig. 12. DVB-S-based passive radar experimental campaign (a) receiving hardware, (b) acquired direct signal power spectral density, and (c) cooperative target side-view photograph.

TABLE IV
DVB-S PASSIVE ISAR EXPERIMENTAL PSF PARAMETERS

Parameter		Value
Receiver bandwidth	B	25 MHz
Central frequency	f_c	11361.75 MHz
Tx aspect angle	θ_T^0	-33.91 deg
Tx elevation angle	ψ_T^0	29.75 deg
Rx aspect angle	θ_R^0	-36.53 deg
Rx elevation angle	ψ_R^0	-0.90 deg
Bistatic angle	β	30.75 deg
Aperture time	T_a	208 ms
Ferry yaw speed	ω_z^0	4.91 deg/s
Ferry pitch speed	ω_y^0	0.27 deg/s
Ferry roll speed	ω_x^0	-0.05 deg/s

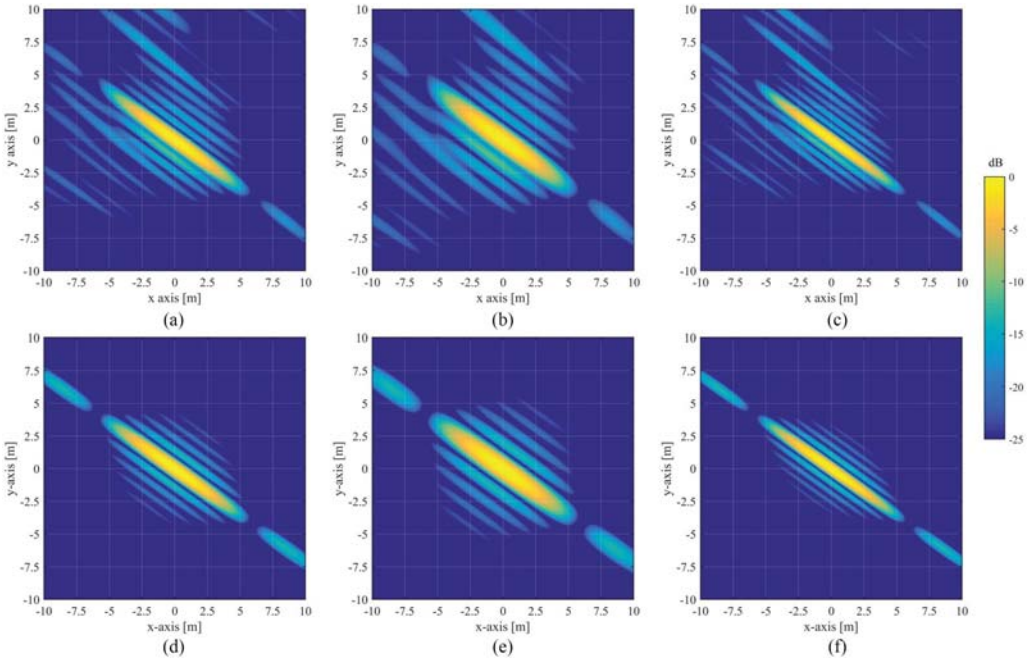

Fig. 13. DVB-S-based passive ISAR PSFs. Experimental images—(a) $\tilde{\omega}_z = \omega_z$. (b) $\tilde{\omega}_z = \omega_z - 0.3\omega_z$. (c) $\tilde{\omega}_z = \omega_z + 0.3\omega_z$. Theoretical images—(d) $\tilde{\omega}_z = \omega_z$. (e) $\tilde{\omega}_z = \omega_z - 0.3\omega_z$. (f) $\tilde{\omega}_z = \omega_z + 0.3\omega_z$.

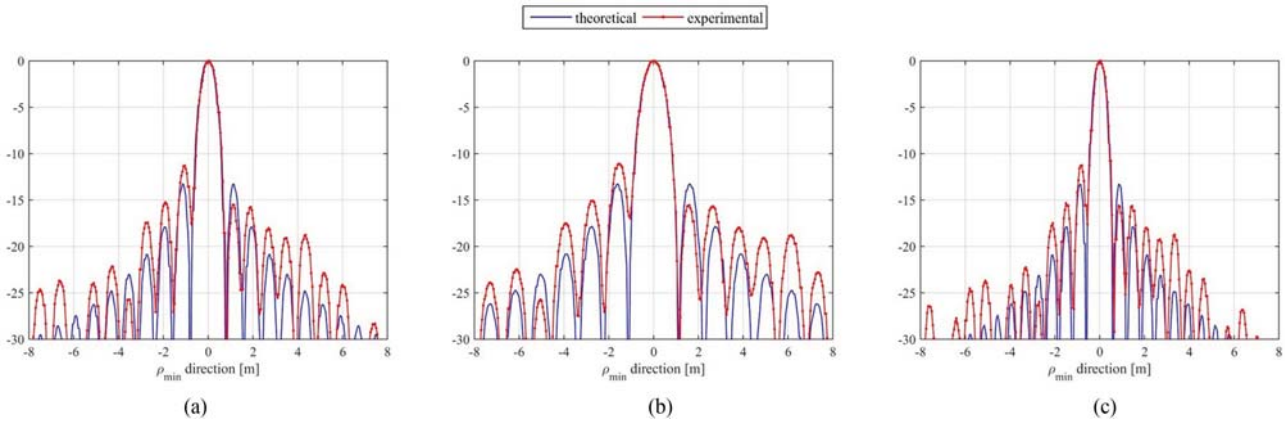

Fig. 14. DVB-S-based passive ISAR PSFs, theoretical and experimental cuts along the $\rho_{\min}$ direction. (a) $\tilde{\omega}_z = \omega_z$. (b) $\tilde{\omega}_z = \omega_z - 0.3\omega_z$. (c) $\tilde{\omega}_z = \omega_z + 0.3\omega_z$.

we focused the image via BPA using three different values of the rotation vector, namely actual motion (as registered by the IMU and reported in Table IV) and by injecting an error of $\pm 30\%$ on the yaw component. Fig. 13 shows the resulting images, where on the top row the experimental PSFs are displayed along with the corresponding theoretical PSFs on the bottom row. A nice correspondence between the experimental and theoretical results can be appreciated for both the ideal and with motion error cases. This correspondence is further confirmed by inspecting the cuts along the $\rho_{\min}$ axis direction shown in Fig. 14.

Table V lists the parameters of a second case study where several scattering points could be observed in the image. In this case, the whole acquired 80 MHz bandwidth has been exploited. It could be shown that even though the spectrum of the signal over this interval includes some gaps, these are sufficiently small and do not produce any grating lobes in the target area and thus do not significantly affect the range response. Particularly, B_{eq} has been measured equal to $\sim$70 MHz. Considering also the target rotation vector and the acquisition geometry, this results in a PSF having a quite fine spatial resolution in all the directions, with a resolution ellipse with $\rho_{\min} \approx 0.4$ m and $\rho_{\text{MAX}} \approx 2.1$ m, therefore with an area of about 70 cm^2. Such a fine resolution potentially allows to identify a number of details of the imaged target and, in particular, may enable target edge identification for a quite accurate target dimension estimation.

Fig. 15(a) shows the top view of the target photograph where the dotted lines highlight a grid to identify different portions of the ferry. Images have been focused via BPA using the nominal value of the rotation vector [see Fig. 15(b)] and injecting an

TABLE V
DVB-S PASSIVE ISAR EXPERIMENTAL IMAGES PARAMETERS

Parameter		Value
Receiver bandwidth	B	80 MHz
Central frequency	f_c	11.347 GHz
Tx aspect angle	θ_T^0	-148.79 deg
Tx elevation angle	ψ_T^0	33.61 deg
Rx aspect angle	θ_R^0	-152.13 deg
Rx elevation angle	ψ_R^0	2.84 deg
Bistatic angle	β	30.93 deg
Aperture time	T_a	838 ms
Ferry yaw speed	ω_z^0	2.08 deg/s
Ferry pitch speed	ω_y^0	0.05 deg/s
Ferry roll speed	ω_x^0	0.01 deg/s

error equal to $\pm 30\%$ on the yaw component [see Fig. 15(c) and (d)]. It could be shown that these errors do not cause significant defocusing because of the limited target size (38). In the ISAR images, 0 dB denotes the mean background power (for the sake of better visualization of the dominant scattering centers, the color dynamic range has been saturated between 5 and 25 dB), while the white dotted lines highlight the same grid sketched in Fig. 15(a). In the ideal image, the points of the grid are located in their nominal positions, whereas in the images focused using erroneous rotation vectors, their positions have been calculated according to the deformation matrix $\boldsymbol{S}_{\tilde{\xi}}$. It can be appreciated as, for both the erroneous values of the yaw speed, the scattering points fit well the areas outlined by the "distorted" grids (see, for example, the bottom right corner where several bright returns can be seen). The distortion of the images will entail an erroneous evaluation of the target edges location that, in turn, affects the capability of measuring its physical dimension, as it can be appreciated by looking at the superimposition of the images over the ferry optical photograph in Fig. 16. It can be seen as, in this case, the underestimation of the rotation speed brought to the larger errors in identifying the ferry's edges than its overestimation. Inspecting, for example, the bottom right corner, we observe that several bright returns are imaged well outside the actual ferry's area when $\tilde{\omega}_z = \omega_z - 0.3\omega_z$ [see Fig. 16(b)], while they still remain inside it for $\tilde{\omega}_z = \omega_z + 0.3\omega_z$ [see Fig. 16(c)].

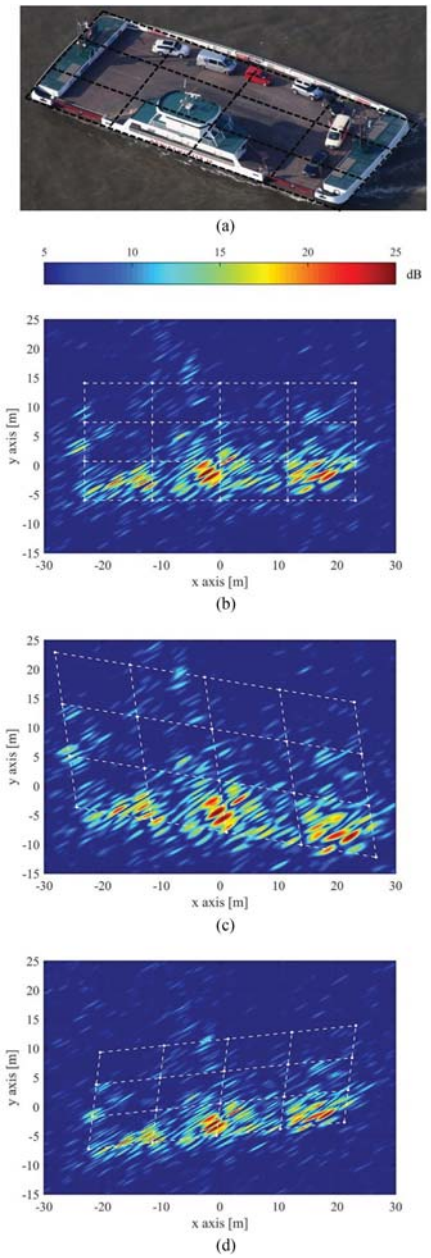

Fig. 15. DVB-S based passive ISAR images. (a) Target grid. (b) Focused image with IMU information. (c) Focused image with $\tilde{\omega}_z = \omega_z - 0.3\omega_z$. (d) Focused image with $\tilde{\omega}_z = \omega_z + 0.3\omega_z$.

VI. CONCLUSION

BPA showed great potential for ISAR image formation, including the possibility of directly extracting the target size from the images and to focus the data without any assumption on the target motion. However, target kinematic parameters needed for the focusing must be generally obtained by data-driven estimation procedures, which could be significantly affected in the passive radar scenario using waveforms not originally intended for imaging procedures. In this work, to achieve a comprehensive understanding of the effects caused by rotational motion estimation errors, a generalized approach able to quantify their impact on the passive ISAR image products has been defined. Particularly, different types of rotational motion estimation errors in general bistatic geometries have been considered and their effects on the PSF and on the image plane have been analytically derived. A few scenarios have been considered to illustrate the effectiveness of the methods in case studies of practical interest. These also include experimental results with terrestrial illuminators in the UHF band and satellite signals in the Ku-band, showing the wide applicability of the proposed methods in different classes of passive systems. This work aims at serving as a tool for passive ISAR users to set proper requirements for the motion estimation task to ensure the image's reliability. Moreover, the provided derivations can be used to build parametric motion estimation procedures. As BPA is particularly suitable for multiangle acquisitions, the next stage of this research is moving from the bistatic to the

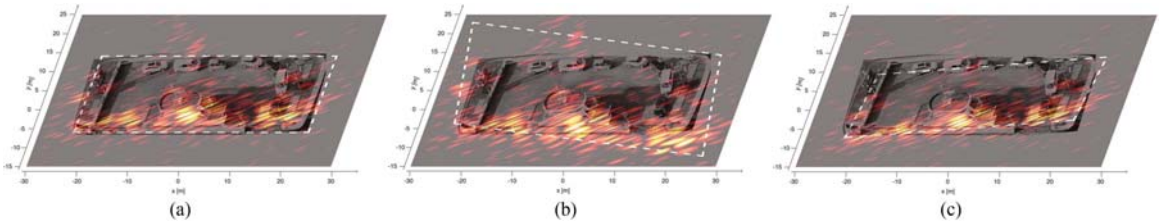

Fig. 16. DVB-S-based passive ISAR images superimposed to the optical photograph for (a) ideal BPA focusing, (b) BPA with $\tilde{\omega}_z = \omega_z - 0.3\omega_z$, and (c) BPA with $\tilde{\omega}_z = \omega_z + 0.3\omega_z$.

multistatic scenario, investigating as motion estimation errors affect multistatic passive ISAR.

Appendix A
Instantaneous Rotation Matrix Derivatives

From the definition of the instantaneous rotation matrix $\boldsymbol{M}_\omega(u)$ in (2), as $\boldsymbol{M}_\gamma^0 = \boldsymbol{M}_\gamma(u=0) = \boldsymbol{I}$ $(\gamma = x, y, z)$, it is easy to see that

$$\dot{\boldsymbol{M}}_\omega = \dot{\boldsymbol{M}}_z + \dot{\boldsymbol{M}}_y + \dot{\boldsymbol{M}}_x = \begin{bmatrix} 0 & -\omega_z^0 & \omega_y^0 \\ \omega_z^0 & 0 & -\omega_x^0 \\ -\omega_y^0 & \omega_x^0 & 0 \end{bmatrix} \tag{A1}$$

$$\ddot{\boldsymbol{M}}_\omega = \ddot{\boldsymbol{M}}_z + \ddot{\boldsymbol{M}}_y + \ddot{\boldsymbol{M}}_x + 2\dot{\boldsymbol{M}}_z\dot{\boldsymbol{M}}_y + 2\dot{\boldsymbol{M}}_z\dot{\boldsymbol{M}}_x + 2\dot{\boldsymbol{M}}_y\dot{\boldsymbol{M}}_x. \tag{A2}$$

We explicitly point out that by means of the skew-symmetric matrix (A1), the cross product in (13) is easily obtained. Carrying out the calculus for (A2), we have

$$\begin{cases} \ddot{\boldsymbol{M}}_x = 2\dot{\omega}_x \begin{bmatrix} 0 & 0 & 0 \\ 0 & 0 & -1 \\ 0 & 1 & 0 \end{bmatrix} - \omega_x^{0\,2} \begin{bmatrix} 0 & 0 & 0 \\ 0 & 1 & 0 \\ 0 & 0 & 1 \end{bmatrix} \\ \ddot{\boldsymbol{M}}_y = 2\dot{\omega}_y \begin{bmatrix} 0 & 0 & 1 \\ 0 & 0 & 0 \\ -1 & 0 & 0 \end{bmatrix} - \omega_y^{0\,2} \begin{bmatrix} 1 & 0 & 0 \\ 0 & 0 & 0 \\ 0 & 0 & 1 \end{bmatrix} \\ \ddot{\boldsymbol{M}}_z = 2\dot{\omega}_z \begin{bmatrix} 0 & -1 & 0 \\ 1 & 0 & 0 \\ 0 & 0 & 0 \end{bmatrix} - \omega_z^{0\,2} \begin{bmatrix} 1 & 0 & 0 \\ 0 & 1 & 0 \\ 0 & 0 & 0 \end{bmatrix} \\ \dot{\boldsymbol{M}}_z\dot{\boldsymbol{M}}_y = 2\dot{\omega}_x \begin{bmatrix} 0 & 0 & 0 \\ 0 & 0 & -1 \\ 0 & 1 & 0 \end{bmatrix} \\ \dot{\boldsymbol{M}}_z\dot{\boldsymbol{M}}_x = 2\dot{\omega}_y \begin{bmatrix} 0 & 0 & 1 \\ 0 & 0 & 0 \\ -1 & 0 & 0 \end{bmatrix} \\ \dot{\boldsymbol{M}}_y\dot{\boldsymbol{M}}_x = 2\dot{\omega}_z \begin{bmatrix} 0 & -1 & 0 \\ 1 & 0 & 0 \\ 0 & 0 & 0 \end{bmatrix} \end{cases}. \tag{A3}$$

Replacing in (A2), $\ddot{\boldsymbol{M}}_\omega$ can be rewritten as

$$\ddot{\boldsymbol{M}}_\omega = \begin{bmatrix} -\omega_y^{0\,2} - \omega_z^{0\,2} & 2\omega_y^0\omega_x^0 & 2\omega_z^0\omega_x^0 \\ 0 & -\omega_x^{0\,2} - \omega_z^{0\,2} & 2\omega_z^0\omega_y^0 \\ 0 & 0 & -\omega_x^{0\,2} - \omega_y^{0\,2} \end{bmatrix} + 2\begin{bmatrix} 0 & -\dot{\omega}_z & \dot{\omega}_y \\ \dot{\omega}_z & 0 & -\dot{\omega}_x \\ -\dot{\omega}_y & \dot{\omega}_x & 0 \end{bmatrix} \tag{A4}$$

so bringing $\ddot{\tau}_{\boldsymbol{a}}$ to be written as in (15).

Appendix B
Deformation Matrix in the Case $\widetilde{\hat{\boldsymbol{\xi}}} = \hat{\boldsymbol{\xi}}$

By replacing $\widetilde{\hat{\boldsymbol{\xi}}}$ with $\hat{\boldsymbol{\xi}}$ and $\omega_{\text{Eff}}/\tilde{\omega}_{\text{Eff}} = \epsilon_\omega$ in (40), the deformation matrix becomes

$$\boldsymbol{S}_\xi = \begin{bmatrix} \hat{\phi}_{\beta_{\setminus z}} \\ \hat{\boldsymbol{\xi}}_{\setminus z} \end{bmatrix}^{-1} \begin{bmatrix} \hat{\phi}_{\beta_{\setminus z}} \\ \epsilon_\omega \hat{\boldsymbol{\xi}}_{\setminus z} \end{bmatrix}. \tag{B1}$$

The second matrix in (B1) can be rewritten as

$$\begin{bmatrix} \hat{\phi}_{\beta_{\setminus z}} \\ \epsilon_\omega \hat{\boldsymbol{\xi}}_{\setminus z} \end{bmatrix} = \begin{bmatrix} \hat{\phi}_{\beta_{\setminus z}} \\ \hat{\boldsymbol{\xi}}_{\setminus z} \end{bmatrix} \det\left\{ \begin{bmatrix} \hat{\phi}_{\beta_{\setminus z}} \\ \hat{\boldsymbol{\xi}}_{\setminus z} \end{bmatrix} \right\}^{-1} \begin{bmatrix} \phi_x\xi_y - \epsilon_\omega\phi_y\xi_x & -\phi_y\xi_y(\epsilon_\omega - 1) \\ \phi_x\xi_x(\epsilon_\omega - 1) & -\phi_y\xi_x + \epsilon_\omega\phi_x\xi_y \end{bmatrix} \tag{B2}$$

where $\det\{*\}$ denotes the determinant of the matrix and ϕ_x and ϕ_y (respectively ξ_x and ξ_y) denote the components of $\hat{\phi}_{\beta_{\setminus z}}$ (respectively $\hat{\xi}_{\setminus z}$). Therefore

$$\boldsymbol{S}_\xi = \left(\phi_x\xi_y - \phi_y\xi_x\right)^{-1} \begin{bmatrix} \phi_x\xi_y - \epsilon_\omega\phi_y\xi_x & -\phi_y\xi_y(\epsilon_\omega - 1) \\ \phi_x\xi_x(\epsilon_\omega - 1) & -\phi_y\xi_x + \epsilon_\omega\phi_x\xi_y \end{bmatrix}. \tag{B3}$$

Recalling that $\alpha_\Theta = \text{tg}^{-1}(\phi_y/\phi_x)$ and $\alpha_\xi = \text{tg}^{-1}(\xi_y/\xi_x)$, some simple manipulations bring to (41).

Appendix C
Deformation Matrix and Position Error for Ground Plane Coinciding With the IPP

In the special case of the ground plane coinciding with the IPP, as the range and azimuth directions are orthogonal over the image, it results $-\theta_x/\theta_y = \xi_y/\xi_x$. Using this position in (B3), the deformation matrix can be simplified as

$$\boldsymbol{S}_\xi^\perp = \begin{bmatrix} \epsilon_\omega\cos^2(\alpha_\xi) + \sin^2(\alpha_\xi) & (\epsilon_\omega - 1)\cos(\alpha_\xi)\sin(\alpha_\xi) \\ (\epsilon_\omega - 1)\cos(\alpha_\xi)\sin(\alpha_\xi) & \epsilon_\omega\sin^2(\alpha_\xi) + \cos^2(\alpha_\xi) \end{bmatrix}. \tag{C1}$$

It is easy to verify that this matrix can be rewritten as the matrix multiplications in (43), which provides a clear geometric interpretation of the procedure to calculate the apparent scatterer position under these special conditions.

The position error (42) in this case can be rewritten as

$$\delta\bar{\boldsymbol{a}}_k^{\perp} = \left(\boldsymbol{M}_{\alpha_\xi}^T \boldsymbol{Q} \boldsymbol{M}_{\alpha_\xi} - \boldsymbol{I}\right) \bar{\boldsymbol{a}}_k. \tag{C2}$$

As in this case $\delta\bar{\boldsymbol{a}}_k^{\perp}$ lies on the azimuth resolution direction, its norm can be easily calculated by applying a clockwise rotation by angle α_ξ to the equation above to transit in the (x', y') reference system, bringing to

$$\begin{aligned} \|\delta\bar{\boldsymbol{a}}_k^{\perp}\| &= \|\left(\boldsymbol{Q} - \boldsymbol{I}\right) \boldsymbol{M}_{\alpha_\xi} \bar{\boldsymbol{a}}_k\| \\ &= \left\| \begin{bmatrix} \epsilon_\omega - 1 & 0 \\ 0 & 0 \end{bmatrix} \boldsymbol{M}_{\alpha_\xi} \begin{bmatrix} \bar{x}_k \\ \bar{y}_k \end{bmatrix} \right\| \\ &= |\epsilon_\omega - 1| \ \left|\bar{x}_k \cos\left(\alpha_\xi\right) + \bar{y}_k \sin\left(\alpha_\xi\right)\right|. \end{aligned} \tag{C3}$$

Therefore, as $|\bar{x}_k \cos(\alpha_\xi) + \bar{y}_k \sin(\alpha_\xi)| = \sqrt{\bar{x}_k^2 + \bar{y}_k^2}\cos(\alpha_\xi - \alpha_k)$, (C3) can be rewritten as (44).

ACKNOWLEDGMENT

The experimental campaign in Livorno (Italy) has been conducted in the context of the project "Multichannel Passive ISAR Imaging for Military Applications (MAPIS)" in the frame of the Project B-1359 IAP2 GP of the European Defense Agency.

REFERENCES

[1] M. Martorella and E. Giusti, "Theoretical foundation of passive bistatic ISAR imaging," *IEEE Trans. Aerosp. Electron. Syst.*, vol. 50, no. 3, pp. 1647–1659, Jul. 2014.

[2] D. Olivadese, E. Giusti, D. Petri, M. Martorella, A. Capria, and F. Berizzi, "Passive ISAR with DVB-T signals," *IEEE Trans. Geosci. Remote Sens.*, vol. 51, no. 8, pp. 4508–4517, Aug. 2013.

[3] W. Feng, J.-M. Friedt, G. Cherniak, and M. Sato, "Passive radar imaging by filling gaps between ISDB digital TV channels," *IEEE J. Sel. Topics Appl. Earth Observ. Remote Sens.*, vol. 12, no. 7, pp. 2055–2068, Jul. 2019.

[4] F. Colone, D. Pastina, and V. Marongiu, "VHF cross-range profiling of aerial targets via passive ISAR: Signal processing schemes and experimental results," *IEEE Trans. Aerosp. Electron. Syst.*, vol. 53, no. 1, pp. 218–235, Feb. 2017.

[5] P. Krysik, K. Kulpa, P. Samczynski, K. Szumski, and J. Misiurewicz, "Moving target detection and imaging using GSM-based passive radar," in *Proc. IET Int. Conf. Radar Syst.*, 2012, pp. 1–4.

[6] F. Colone, D. Pastina, P. Falcone, and P. Lombardo, "WiFi-based passive ISAR for high-resolution cross-range profiling of moving targets," *IEEE Trans. Geosci. Remote Sens.*, vol. 52, no. 6, pp. 3486–3501, Jun. 2014.

[7] D. Pastina, F. Colone, T. Martelli, and P. Falcone, "Parasitic exploitation of wi-fi signals for indoor radar surveillance," *IEEE Trans. Veh. Technol.*, vol. 64, no. 4, pp. 1401–1415, Apr. 2015.

[8] S. Brisken, M. Moscadelli, V. Seidel, and C. Schwark, "Passive radar imaging using DVB-S2," in *Proc. IEEE Radar Conf.*, 2017, pp. 552–556.

[9] I. Pisciottano, F. Santi, D. Pastina, and D. Cristallini, "DVB-S based passive polarimetric ISAR – Methods and experimental validation," *IEEE Sensor J.*, vol. 21, no. 5, pp. 6056–6070, Mar. 2021.

[10] T. V. Cao, R. Melino, and H.-T. Tran, "Using passive ISAR for imaging maritime targets," in *Proc. 20th Int. Radar Symp.*, 2019, pp. 1–10.

[11] S. Gutierrez-Serrano, M.-C. Benito-Ortiz, D. Mata-Moya, M.-P. Jarabo-Amores, and N. Del-Rey-Maestre, "Road traffic passive radar imaging using DVB-S," in *Proc. 23rd Int. Radar Symp.*, 2022, pp. 218–223.

[12] D. Pastina, F. Santi, F. Pieralice, M. Antoniou, and M. Cherniakov, "Passive radar imaging of ship targets with GNSS signals of opportunity," *IEEE Trans. Geosci. Remote Sens.*, vol. 59, no. 3, pp. 2627–2642, Mar. 2021.

[13] J. L. Garry and G. E. Smith, "Passive ISAR part I: Framework and considerations," *IET Radar Sonar Navigation*, vol. 13, no. 2, pp. 169–180, Feb. 2019.

[14] M. K. Bączyk and K. Kulpa, "Moving target imaging in multistatic passive radar," *IET Radar Sonar Navigation*, vol. 13, no. 2, pp. 198–207, Feb. 2019.

[15] F. Santi, D. Pastina, M. Antoniou, and M. Cherniakov, "GNSS-based multistatic passive radar imaging of ship targets," in *Proc. IEEE Int. Radar Conf.*, 2020, pp. 601–606.

[16] C. Huang, Z. Li, H. An, Z. Sun, J. Wu, and J. Yang, "Passive multistatic radar imaging of vessel target using GNSS satellites of opportunity," *IEEE Trans. Geosci. Remote Sens.*, vol. 60, 2022, Art. no. 5116416.

[17] P. Wang, X. Zhou, Y. Fang, H. Zeng, and J. Chen, "GNSS-based passive inverse SAR imaging," *IEEE J. Sel. Topics Appl. Earth Observ. Remote Sens.*, vol. 16, pp. 508–521, 2023.

[18] J. L. Garry and G. E. Smith, "Passive ISAR Part II: Narrowband imaging," *IET Radar Sonar Navigation*, vol. 13, no. 2, pp. 181–189, Feb. 2019.

[19] F. Santi, I. Pisciottano, D. Pastina, and D. Cristallini, "First experimental results on multi-angle DVB-S based passive ISAR exploiting multipolar data," in *Proc. IEEE Radar Conf.*, 2021, pp. 1–6.

[20] I. Pisciottano, D. Cristallini, and D. Pastina, "Maritime target imaging via simultaneous DVB-T and DVB-S passive ISAR," *IET Radar Sonar Navigation*, vol. 13, no. 9, pp. 1479–1487, Sep. 2019.

[21] F. Santi, I. Pisciottano, D. Pastina, and D. Cristallini, "Impact of motion estimation errors on DVB-S based passive ISAR imaging," in *Proc. IEEE Radar Conf.*, 2022, pp. 1–6.

[22] M. Martorella, J. Palmer, J. Homer, B. Littleton, and I. D. Longstaff, "On bistatic inverse synthetic aperture radar," *IEEE Trans. Aerosp. Electron. Syst.*, vol. 43, no. 3, pp. 1125–1134, Jul. 2007.

[23] M. Martorella, "Analysis of the robustness of bistatic inverse synthetic aperture radar in the presence of phase synchronization errors," *IEEE Trans. Aerosp. Electron. Syst.*, vol. 47, no. 4, pp. 2673–2689, Oct. 2011.

[24] B.-S. Kang, B.-H. Ryu, and K.-T. Kim, "Bistatic ISAR imaging for nonuniformly rotating targets," *IEEE Trans. Aerosp. Electron. Syst.*, vol. 55, no. 4, pp. 1972–1988, Aug. 2019.

[25] T. Zeng, M. Cherniakov, and T. Long, "Generalized approach to resolution analysis in BSAR," *IEEE Trans. Aerosp. Electron. Syst.*, vol. 41, no. 2, pp. 461–474, Apr. 2005.

[26] F. Daout, F. Schmitt, G. Ginolhac, and P. Fargette, "Multistatic and multiple frequency imaging resolution analysis – Application to GPS-based multistatic radar," *IEEE Trans. Aerosp. Electron. Syst.*, vol. 48, no. 4, pp. 3042–3057, Oct. 2012.

[27] Y. Wang, "Inverse synthetic aperture radar imaging of manoeuvring target based on range-instantaneous-Doppler and range-instantaneous-chirp-rate algorithms," *IET Radar Sonar Navigation*, vol. 6, no. 9, pp. 921–928, Dec. 2012.

[28] A. W. Doerry and D. L. Bickel, "Synthetic aperture radar height of focus," Sandia Nat. Lab., Albuquerque, NM, USA, SANDIA Rep. SAND2021-144, Jan. 2021.

[29] A. Manno-Kovacs, E. Giusti, F. Berizzi, and L. Kovács, "Image based robust target classification for passive ISAR," *IEEE Sensors J.*, vol. 19, no. 1, pp. 268–276, Jan. 2019.

[30] A. Kurowska, J. S. Kulpa, E. Giusti, and M. Conti, "Classification results of ISAR sea targets based on their two features," in *Proc. Signal Process. Symp.*, 2017, pp. 1–6.

[31] A. W. Doerry, "Ship dynamics for maritime ISAR imaging," SANDIA, Albuquerque, NM, USA, Rep. SAND2008-1020, Feb. 2008.

[32] Q. Zhang, T. S. Yeo, G. Du, and S. Zhang, "Estimation of three-dimensional motion parameters in interferometric ISAR imaging," *IEEE Trans. Geosci. Remote Sens.*, vol. 42, no. 2, pp. 292–300, Feb. 2004.

[33] K. Suwa, T. Wakayama, and M. Iwamoto, "Three-dimensional target geometry and target motion estimation method using multistatic ISAR movies and its performance," *IEEE Trans. Geosci. Remote Sens.*, vol. 49, no. 6, pp. 2361–2373, Jun. 2011.

[34] G. Xu, M. Xing, X.-G. Xia, L. Zhang, Q. Chen, and Z. Bao, "3D geometry and motion estimations of maneuvering targets for interferometric ISAR with sparse aperture," *IEEE Trans. Image Process.*, vol. 25, no. 5, pp. 2005–2020, May 2016.

[35] F. Santi, M. Bucciarelli, and D. Pastina, "Multi-sensor ISAR technique for feature-based motion estimation of ship targets," in *Proc. Int. Radar Conf.*, 2014, pp. 1–5.

[36] F. Santi, D. Pastina, and M. Bucciarelli, "Estimation of ship dynamics with a multiplatform radar imaging system," *IEEE Trans. Aerosp. Electron. Syst.*, vol. 53, no. 6, pp. 2769–2788, Dec. 2017.

[37] F. Rice, T. Cooke, and D. Gibbins, "Model based ISAR ship classification," *Digit. Signal Process.*, vol. 16, no. 5, pp. 628–637, 2006.

[38] F. Filippini, O. Cabrera, C. Bongioanni, F. Colone, and P. Lombardo, "DVB-S based passive radar for short range security application," in *Proc. IEEE Radar Conf.*, 2021, pp. 1–6.

[39] J. Li et al., "A DVB-S-based multichannel passive radar system for vehicle detection," *IEEE Access*, vol. 9, pp. 2900–2912, 2021.

[40] N. Del-Rey-Maestre, M. P. Jarabo-Amores, D. Mata-Moya, A. Almódovar-Hernández, and J. Rosado-Sanz, "Planar array and spatial filtering techniques for improving DVB-S based passive radar coverage," in *Proc. 19th Eur. Radar Conf.*, 2022, pp. 1–4.
[41] ASTRA 1KR, Accessed: Dec. 29, 2022. [Online]. Available: https://www.ses.com/our-coverage#/explore/satellite/335
[42] Z. Sun, T. Wang, T. Jiang, C. Chen, and W. Chen, "Analysis of the properties of DVB-S signal for passive radar applications," in *Proc. Int. Conf. Wireless Commun. Signal Process.*, 2013, pp. 1–5.

Fabrizio Santi (Member, IEEE) received the master's degree (*cum laude*) in telecommunication engineering and the Ph.D. degree in remote sensing from the Sapienza University of Rome, Rome, Italy, in 2010 and 2014, respectively.

From April 2013 to September 2013, he carried out research activity with the Microwave Integrated Systems Laboratory, University of Birmingham, U.K. He is currently an Assistant Professor with the Department of Information Engineering, Electronics and Telecommunications, Sapienza University of Rome. He is an author/coauthor of more than 50 publications in peer-reviewed international journals and conferences. His main research interests include bi/multistatic SAR/ISAR techniques, passive coherent location radar systems, and multidimensional passive radar imaging. He was involved in scientific research projects funded by the European Commission, the Italian Space Agency, the European Space Agency, and the national radar industry.

Dr. Santi is a member of the Editorial Board of the *International Journal of Electronics and Communications* (AEÜ, Elsevier) and he also serves as an Associate Editor for IEEE ACCESS and IEEE SENSORS JOURNAL.

Iole Pisciottano received the master's degree in telecommunication engineering from the "Federico II" University of Naples, Naples, Italy, in 2011, and the Ph.D. degree in radar and remote sensing from the University of Rome "La Sapienza," Rome, Italy, in 2021.

From June 2010 to December 2010, she carried out research activity with the Polarimetric SAR Interferometry (Pol-InSAR) Group, DLR Microwaves and Radar Institute, Germany. From 2011 to 2014, she was a Research Scientist with the Ultra-Wide Band Team in the Passive Radar Anti Jamming Techniques and Classification Department, Fraunhofer Institute for High Frequency Physics and Radar Techniques FHR, Wachtberg, Germany. Since 2017, she has been with the Passive Covert Radar Team in the Passive Radar and Anti-Jamming Techniques Department, now the Department of Signal Processing and Imaging Radar, Fraunhofer Institute FHR. She is involved in scientific research projects funded by the European Defense Agency and European Defense Fund. Her research interests include active and passive SAR and ISAR image processing as well as polarimetry techniques.

Diego Cristallini received the graduate degree (*cum laude*) in telecommunication engineering and the Ph.D. degree in radar remote sensing both from the University of Rome "La Sapienza," Rome, Italy, in 2006 and 2010, respectively.

From 2009 to 2015, he was with the Array-Based Radar Imaging Department, Fraunhofer Institute for High Frequency Physics and Radar Techniques FHR, Wachtberg, Germany. Since 2015, he has been the Head of the Team on Passive Covert Radar in the Passive Radar and Anti-Jamming Techniques Department of Fraunhofer FHR, Germany. From March 2020 to June 2020, he was a Visiting Scientist with the Defence Science and Technology (DST) Group, Edinburgh, South Australia. He serves as a voluntary Reviewer for a number of international technical journals, and he is active in the scientific community serving as TPC for several international conferences related to radar. He is also a Regular Lecturer with the Fraunhofer International Summer School on Radar and SAR. In 2023, he also edited the book *Passive Radar on Moving Platforms* (IET SciTech).

Dr. Cristallini was a Cochair of the NATO-SET 242 Group on "PCL on Moving Platforms" and a Lecturer of the NATO LS-299 "Passive Radar Technology." He was a recipient of the Best Paper Award at EUSAR 2014, coauthored the Best Poster Award at EUSAR 2018, and he was a corecipient of the 2018 Premium Award for Best Paper in IET Radar, Sonar and Navigation.

Debora Pastina (Member, IEEE) received the Laurea degree in telecommunications engineering and the Ph.D. degree in information and communication engineering from the Sapienza University of Rome, Rome, Italy, in 1996 and 2000, respectively.

From 1998 to 1999, she carried on research activity with the SAR Processing Team, Defense Evaluation Research Agency, Malvern, U.K. In March 2001, she joined as an Assistant Professor with the Department of DIET, University of Rome "La Sapienza," where she is currently an Associate Professor teaching several courses related to remote sensing and telecommunications. She is involved and is responsible for scientific research projects funded by the Italian Ministry of Research, the Italian Space Agency, the European Commission, and the national radar industry. The results of her research activity have been reported in a number of journals and conference papers. Her main research interests include SAR/ISAR signal processing, ground moving target indication techniques, GNSS-based passive radar systems, FSR systems, clutter models, coherent and incoherent radar detection in non-Gaussian clutter, and CFAR radar techniques.

Dr. Pastina was the Chairman of the Local Committee of the IEEE/ISPRS Joint Workshop on Remote Sensing and Data Fusion over Urban Areas (Rome, November 2001). She was the Publication Chair of the 2008 IEEE Radar Conference held in Rome in May 2008. She was the Technical Chair of EuRAD 2022 held in Milan in September 2022. She was a member of the Editorial Board of the *International Journal of Electronics and Communications* (AEÜ, Elsevier) acting as an Area Editor for radar systems and techniques (2012–2023). Since 2017, she has been an Associate Editor for Radar Systems for IEEE TRANSACTIONS ON AEROSPACE AND ELECTRONIC SYSTEMS, and since 2023, an Associate Editor for IEEE TRANSACTIONS ON RADAR SYSTEMS.

Open Access funding provided by 'Università degli Studi di Roma "La Sapienza" 2' within the CRUI CARE Agreement